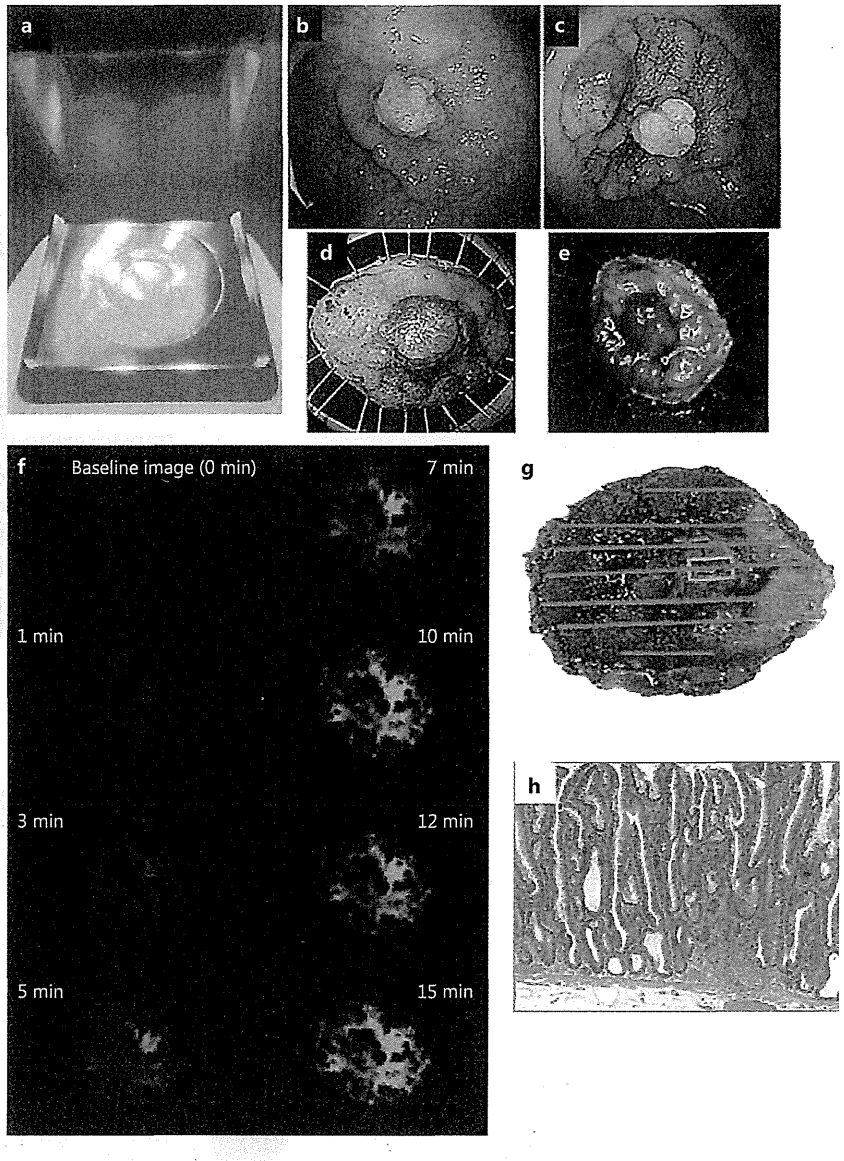

Fig. 1. a The Discovery machine (INDEC Inc.), which provides fluorescent images (emission wavelength >520 nm by long-pass filter) by blue-light (450–490 nm) excitation, with which the baseline and fluorescent images were taken. **b**, **c** White-light image and chromoendoscopic image: the endoscopic diagnosis was Ra, 0-Is+IIa (LST-G), 40 mm in size, cTis. **d** Endoscopic white-light image of a resected specimen. **e** White-light image of a resected specimen taken by Discovery. **f** Fluorescent images after spraying gGlu-HMRG with blue light; rapid fluorescent increase was observed in the tumor regions. **g** Purple lines on histological mapping showed tubular adenocarcinoma. **h** Histological finding of the blue box on the histological mapping indicated colonic well-differentiated tubular adenocarcinoma. HE stain. ×40.

Fluorescent Activity

Twenty (67%) of the images were fluorescently positive for the tumor region after 15 min, and 10 (33%) were negative. The mean tumor sizes in the positive and negative groups were 42 and 32 mm, respectively. Of the 13 adenomas, 7 (54%) lesions were positive and 6 (46%) were negative. Of the 17 carcinomas in adenomas, 13 (76%) lesions showed positive fluorescence and 4 (24%) were negative. According to the macroscopic type, 16 LST-G lesions (80%) and 4 LST-NG lesions (40%) were positive (table 2). Eighteen (75%) of 24 lesions were positive in 50 μM gGlu-HMRG, and 2 (33%) of 6 lesions were positive in 500 μM. Among the 17 carcinomas in adenoma, 12 (80%) of 15 lesions were positive in 50 μM and 1 (50%) of 2 lesions was positive in 500 μM. No histological tissue damage by gGlu-HMRG was seen in any of the resected specimens. Of the 20 positive lesions, some showed a heterogeneous fluorescent increase in the tumor region. An example case was an LST-G lesion 40 mm in size located in the upper rectum. This lesion was removed by ESD. The resected specimen was fixed on a black board and baseline images were obtained. A rapid and heterogeneous fluorescent increase was

Table 1. Clinicopathological characteristics of colorectal tumors (n = 30)

Age, years	68 ± 7
Sex	
Male	15
Female	15
Location	
Right colon	15
Left colon	9
Rectum	6
Endoscopic treatment	
ESD	27
Endoscopic mucosal resection	3
Size, mm	39±13
Macroscopic type	
LST-G	20
LST-NG	10
Histology	
Adenoma	13
Carcinoma in adenoma	17
GGT fluorescent activity	
Positive	20 (67)
Negative	10 (33)

Values are mean ± SD or number with percentage in parentheses.

Table 2. Fluorescent imaging of colorectal lesions with gGlu-HMRG

	Positive (n = 20)	Negative (n = 10)
Size, mm	42±11	32±1
Macroscopic type		
LST-G (n = 20)	16 (80)	4 (20)
LST-NG (n = 10)	4 (40)	6 (60)
Histology		
Adenoma (n = 13)	7 (54)	6 (46)
Carcinoma in adenoma (n = 17)	13 (76)	4 (24)

Values are mean ± SD or number with percentage in parentheses.

observed in the tumor regions after spraying gGlu-HMRG. The histological diagnosis was of a well-differentiated tubular adenocarcinoma, pTis, ly0, v0, VM0, HM0 (fig. 1b–h). One 40-mm LST-G lesion located in the cecum was also removed by ESD. This lesion had a positive fluorescent activity in a tiny area after spraying gGlu-HMRG. The histological diagnosis was of a well-differentiated tubular adenocarcinoma in adenoma, pTis, ly0, v0, VM0, HM0, and the distribution of the adenocarcinoma component on histological mapping was approximately consistent with the tiny area of positive fluorescent activity (fig. 2).

Discussion

GGT expression is considered to be associated with a 'resistance phenotype' exhibited by preneoplastic transformed cells [18]. GGT is overexpressed in various human cancer types in vivo [19–21] and is therefore considered to be a potential biomarker for early cancer detection. This association between GGT and neoplastic transformation was highlighted in several experimental models of chemical carcinogenesis in laboratory animals [18]. The previous literature showed that GGT activity was organ dependent, and the activity was high in several cancer cells, such as the lung, ovary, liver and bile duct [19–21]. Urano [29] reported that GGT fluorescent activity was significantly enhanced to about 60% of the cultured cancer cells. Mitsunaga et al. [23] also reported that gGlu-HMRG could improve endoscopic detection of colitis-associated colon cancer in a mouse model of ulcerative colitis.

In this study, we successfully observed tumor regions as being fluorescently positive by topically spraying of gGlu-HMRG. This method showed a rapid and specific fluorescent increase upon reaction with GGT without any histological tissue damage in an ex vivo model. This is a valuable finding relating to the ex vivo fluorescent imaging of human colorectal LSTs.

Generally, two major categories of fluorescent probes have been used in molecular imaging: 'always-on' and 'activatable'. Always-on probes, such as positron emission tomography, have the disadvantage of high background signal, which requires considerable time to clear to achieve adequate target-to-background ratios. On the other hand, several activatable probes, such as cathepsins, have lower background signal, but the activation process often requires hours to days, impeding the practicality for real-time clinical use in endoscopy [30].

In the present study, overall GGT fluorescent activity was positive in 67% of the specimens. Lesions with a carcinoma component were characterized by higher fluorescence than those with an adenoma component alone, which might imply that there was a relationship between the malignant potential of the cells and GGT fluorescent activity. In addition, some lesions with positive GGT activity revealed heterogeneous fluorescent activity (fig. 1b–h). This might be associated with a histological heteroge-

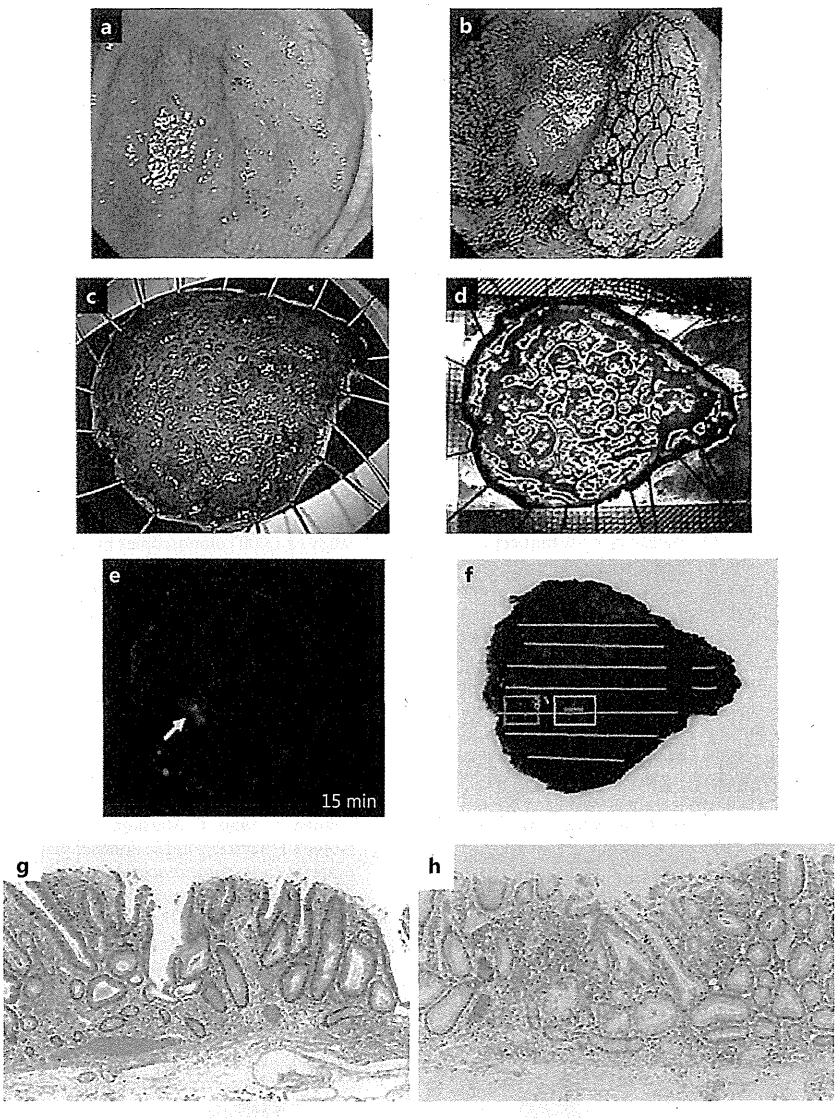

Fig. 2. a, b White-light image and chromoendoscopic image: the endoscopic diagnosis was cecum, 0-IIa (LST-G), 40 mm in size, cTis. **c** Endoscopic white-light image of a resected specimen. **d** White-light image of a resected specimen taken by Discovery. **e** Fluorescent images after spraying gGlu-HMRG with blue light; positive fluorescent activity was seen in a tiny area, as shown by the yellow arrow. **f** Histological mapping: the green lines show tubular adenoma and the narrow range of purple lines show tubular adenocarcinoma. **g** Histological finding of the blue box on the histological mapping indicated colonic adenoma. HE stain. ×40. **h** Histological finding of the yellow box on the histological mapping indicated colonic well-differentiated tubular adenocarcinoma. The distribution of the adenocarcinoma component on histological mapping was approximately consistent with a partially positive GGT fluorescent activity. HE stain. ×40.

neity between adenoma and adenocarcinoma due to the well-known adenoma-carcinoma sequence. Some lesions showed partial GGT fluorescent activity and we experienced an interesting case of intramucosal adenocarcinoma in adenoma (fig. 2). This case showed that the partially positive fluorescent activity and positive area was approximately consistent with the adenocarcinoma component.

This was a pilot study using ex vivo specimens and did not show significant clinical features associated with positive fluorescent imaging by gGlu-HMRG spraying. In addition, the study used two gGlu-HMRG concentrations of 50 and 500 μM. Of 17 carcinomas in adenomas, the proportion of positive fluorescent activity in 50 and 500 μM were 80% (12/15 lesions) and 50% (1/2 lesions), respectively. Given the small samples, it was difficult to analyze the differences in fluorescent increase between the two gGlu-HMRG concentrations. Further investigation is needed to confirm the safety and feasibility of this technique in humans prior to the future application of this fluorescent imaging for clinical diagnosis.

In conclusion, topically spraying gGlu-HMRG enabled rapid and selective fluorescent imaging of colorectal tumors owing to the upregulated GGT activity in cancer cells.

Acknowledgement

This study was supported by the National Cancer Center Research and Development Fund (23-B-17). We wish to express our appreciation to Klaus Mönkemüller, MD, PhD, FASGE (Basil I. Hirschowitz Endoscopic Center of Excellence, Division of Gastroenterology and Hepatology, University of Alabama at Birmingham, Ala., USA) for his generous assistance in editing this manuscript.

Disclosure Statement

The authors have no commercial association that might be a conflict of interest in relation to our submitted manuscript.

References

1 Pox CP: Controversies in colorectal cancer screening. Digestion 2014;89:274–281.
2 Nishihara R, Wu K, Lochhead P, Morikawa T, Liao X, Qian ZR, Inamura K, Kim SA, Kuchiba A, Yamauchi M, Imamura Y, Willett WC, Rosner BA, Fuchs CS, Giovannucci E, Ogino S, Chan AT: Long-term colorectal-cancer incidence and mortality after lower endoscopy. N Engl J Med 2013;369:1095–1105.
3 Shaukat A, Mongin SJ, Geisser MS, Lederle FA, Bond JH, Mandel JS, Church TR: Long-term mortality after screening for colorectal cancer. N Engl J Med 2013;369:1106–1114.
4 Brooker JC, Saunders BP, Shah SG, Thapar CJ, Thomas HJ, Atkin WS, et al: Total colonic dye-spray increases the detection of diminutive adenomas during routine colonoscopy: a randomized controlled trial. Gastrointest Endosc 2002;56:333–338.
5 Fujii T, Hasegawa RT, Saitoh Y, Fleischer D, Saito Y, Sano Y, Kato S: Chromoscopy during colonoscopy. Endoscopy 2001;33:1036–1041.
6 Sano Y, Ikematsu H, Fu KI, Emura F, Katagiri A, Horimatsu T, Kaneko K, Soetikno R, Yoshida S: Meshed capillary vessels by use of narrow-band imaging for differential diagnosis of small colorectal polyps. Gastrointest Endosc 2009;69:278–283.
7 Uraoka T, Saito Y, Matsuda T, Sano Y, Ikehara H, Mashimo Y, et al: Detectability of colorectal neoplastic lesions using a narrow-band imaging system: a pilot study. J Gastroenterol Hepatol 2008;23:1810–1815.
8 Matsuda T, Saito Y, Fu KI, Uraoka T, Kobayashi N, Nakajima T, Ikehara H, Mashimo Y, Shimoda T, Murakami Y, Parra-Blanco A, Fujimori T, Saito D: Does autofluorescence imaging videoendoscopy system improve the colonoscopic polyp detection rate? A pilot study. Am J Gastroenterol 2008;103:1926–1932.
9 Shahid MW, Buchner AM, Heckman MG, Krishna M, Raimondo M, Woodward T, Wallace MB: Diagnostic accuracy of probe-based confocal laser endomicroscopy and narrow band imaging for small colorectal polyps: a feasibility study. Am J Gastroenterol 2012;107:231–239.
10 Fujii T, Rembacken BJ, Dixon MF, Yoshida S, Axon AT: Flat adenomas in the United Kingdom: are treatable cancers being missed? Endoscopy 1998;30:437–443.
11 Rembacken BJ, Fujii T, Cairns A, Dixon MF, Yoshida S, Chalmers DM, Axon AT: Flat and depressed colonic neoplasms: a prospective study of 1,000 colonoscopies in the UK. Lancet 2000;355:1211–1214.
12 Tsuda S, Veress B, Tóth E, Fork FT: Flat and depressed colorectal tumours in a southern Swedish population: a prospective chromoendoscopic and histopathological study. Gut 2002;51:550–555.
13 Tamura S, Nakajo K, Yokoyama Y, Ohkawauchi K, Yamada T, Higashidani Y, Miyamoto T, Ueta H, Onishi S: Evaluation of endoscopic mucosal resection for laterally spreading rectal tumors. Endoscopy 2004;36:306–312.
14 Uraoka T, Saito Y, Matsuda T, Ikehara H, Gotoda T, Saito D, Fujii T: Endoscopic indications for endoscopic mucosal resection of laterally spreading tumours in the colorectum. Gut 2006;55:1592–1597.
15 Saito Y, Fujii T, Kondo H, Mukai H, Yokota T, Kozu T, Saito D: Endoscopic treatment for laterally spreading tumors in the colon. Endoscopy 2001;33:682–686.
16 Saito Y, Uraoka T, Yamaguchi Y, Hotta K, Sakamoto N, Ikematsu H, Fukuzawa M, Kobayashi N, Nasu J, Michida T, Yoshida S, Ikehara H, Otake Y, Nakajima T, Matsuda T, Saito D: A prospective, multicenter study of 1,111 colorectal endoscopic submucosal dissections (with video). Gastrointest Endosc 2010;72:1217–1225.
17 Frangioni JV: New technologies for human cancer imaging. J Clin Oncol 2008;26:4012–4021.
18 Pompella A, de Tata V, Paolicchi A, Zunino F: Expression of γ-glutamyltransferase in cancer cells and its significance in drug resistance. Biochem Pharmacol 2006;71:231–238.
19 Hanigan MH, Frierson HF Jr, Brown JE, Lovell MA, Taylor PT: Human ovarian tumors express γ-glutamyl transpeptidase. Cancer Res 1994;54:286–290.
20 Yao D, Jiang D, Huang Z, Lu J, Tao Q, Yu Z, Meng X: Abnormal expression of hepatoma specific γ-glutamyl transferase and alteration of γ-glutamyl transferase gene methylation status in patients with hepatocellular carcinoma. Cancer 2000;88:761–769.
21 Schäfer C, Fels C, Brucke M, Holzhausen HJ, Bahn H, Wellman M, Visvikis A, Fischer P, Rainov NG: γ-Glutamyl transferase expression in higher-grade astrocytic glioma. Acta Oncol 2001;40:529–535.
22 Urano Y, Sakabe M, Kosaka N, Ogawa M, Mitsunaga M, Asanuma D, Kamiya M, Young MR, Nagano T, Choyke PL, Kobayashi H: Rapid cancer detection by topically spraying a γ-glutamyltranspeptidase-activated fluorescent probe. Sci Transl Med 2011;3:110ra119.
23 Mitsunaga M, Kosaka N, Choyke PL, Young MR, Dextras CR, Saud SM, Colburn NH, Sakabe M, Nagano T, Asanuma D, Urano Y, Kobayashi H: Fluorescence endoscopic detection of murine colitis-associated colon cancer by topically applied enzymatically rapid-activatable probe. Gut 2013;62:1179–1186.
24 Urano Y, Asanuma D, Hama Y, Koyama Y, Barrett T, Kamiya M, Nagano T, Watanabe T, Hasegawa A, Choyke PL, Kobayashi H: Selective molecular imaging of viable cancer cells with pH-activatable fluorescence probes. Nat Med 2009;15:104–109.
25 Munjal DD: Concurrent measurements of carcinoembryonic antigen, glucosephosphate isomerase, γ-glutamyltransferase, and lactate dehydrogenase in malignant, normal adult, and fetal colon tissues. Clin Chem 1980;26:1809–1812.
26 Kudo S, Kashida H, Nakajima T, Tamura S, Nakajo K: Endoscopic diagnosis and treatment of early colorectal cancer. World J Surg 1997;21:694–701.
27 Kudo S, Kashida H, Tamura T, Kogure E, Imai Y, Yamano H, Hart AR: Colonoscopic diagnosis and management of nonpolypoid early colorectal cancer. World J Surg 2000;24:1081–1090.
28 Japanese Society for Cancer of the Colon and Rectum: Japanese Classification of Colorectal Carcinoma, ed 8. Tokyo, Kanehara Shuppan, 2013.
29 Urano Y: In vivo cancer detection with a newly designed fluorescent probe (in Japanese). Gan To Kagaku Ryoho 2013;40:299–303.
30 Kobayashi H, Ogawa M, Alford R, Choyke PL, Urano Y: New strategies for fluorescent probe design in medical diagnostic imaging. Chem Rev 2010;110:2620–2640.

Induction of amphiregulin by p53 promotes apoptosis via control of microRNA biogenesis in response to DNA damage

Naoe Taira[a], Tomoko Yamaguchi[a], Junko Kimura[b], Zheng-Guang Lu[b], Shinji Fukuda[c], Shigeki Higashiyama[c], Masaya Ono[d], and Kiyotsugu Yoshida[a,1]

[a]Department of Biochemistry, The Jikei University School of Medicine, 3-25-8 Nishi-shinbashi, Minato-ku, Tokyo 105-8461, Japan; [b]Medical Research Institute, Tokyo Medical and Dental University, 1-5-45 Yushima, Bunkyo-ku, Tokyo 113-8510, Japan; [c]Department of Chemistry and Molecular Genetics, Ehime University Graduate School of Medicine, Shitsukawa, Toon, Ehime 791-0295, Japan; and [d]Chemotherapy Division and Cancer Proteomics Project, National Cancer Center Research Institute, 5-1-1 Tsukiji, Chuo-ku, Tokyo 104-0045, Japan

Edited by Moshe Oren, Weizmann Institute of Science, Rehovot, Israel, and accepted by the Editorial Board December 11, 2013 (received for review July 20, 2013)

Upon DNA damage, tumor suppressor p53 determines cell fate by repairing DNA lesions to survive or by inducing apoptosis to eliminate damaged cells. The decision is based on its posttranslational modifications. Especially, p53 phosphorylation at Ser46 exerts apoptotic cell death. However, little is known about the precise mechanism of p53 phosphorylation on the induction of apoptosis. Here, we show that amphiregulin (AREG) is identified for a direct target of Ser46 phosphorylation via the comprehensive expression analyses. Ser46-phosphorylated p53 selectively binds to the promoter region of AREG gene, indicating that the p53 modification changes target genes by altering its binding affinity to the promoter. Although AREG belongs to a family of the epidermal growth factor, it also emerges in the nucleus under DNA damage. To clarify nuclear function of AREG, we analyze AREG-binding proteins by mass spectrometry. AREG interacts with DEAD-box RNA helicase p68 (DDX5). Intriguingly, AREG regulates precursor microRNA processing (i.e., miR-15a) with DDX5 to reduce the expression of antiapoptotic protein Bcl-2. These findings collectively support a mechanism in which the induction of AREG by Ser46-phosphorylated p53 is required for the microRNA biogenesis in the apoptotic response to DNA damage.

microarray | Drosha | miRNA processing

Homeostasis is maintained by a balance between cell proliferation and cell death. Activation of oncogenic transcription factor (e.g., c-Myc) and growth factor [e.g., epidermal growth factor (EGF) family proteins] destroys the balance, leading to tumorigenesis. EGF family contains transforming growth factor α (TGF-α), heparin binding-EGF, and amphiregulin (AREG). These growth factors are catalyzed by matrix metalloproteases (MMPs) at the plasma membrane, which enables them to act as a ligand for EGF receptor (EGFR) (1). MMPs are frequently overexpressed in tumors, suggesting that EGF family proteins, besides AREG, mainly function as tumor facilitators. In this context, AREG is exerted as a bifunctional growth modulator (2). However, a mechanism for AREG-mediated growth suppression remains unclear. AREG is initially synthesized as a pro-AREG that encodes 252 aa. Pro-AREG is translocated to the cell surface and then processed by one of MMPs, ADAM17. Soluble AREG directly binds to EGFR as a ligand to transmit growth signal (3). However, AREG is not able to activate EGFR signaling effectively compared with other EGFR ligands (4). It is well established that AREG translocates to the plasma membrane; however, few reports showed that AREG localizes in the nucleus (5, 6). Recent study has demonstrated that AREG translocates to the inner nuclear membrane by a retrograde trafficking and attenuates global transcription (7). Taken together, AREG has multiple functions not only as a ligand for EGFR.

Tumor suppressor p53 transactivates numerous target genes in response to DNA damage to prevent tumorigenesis. The target genes exhibit diverse functions including cell cycle arrest, DNA damage repair, or apoptosis induction (8). The intracellular functions and localization of p53 are regulated by its posttranslational modifications. Especially, Ser46 phosphorylation is a key modification to eliminate cancer cells by inducing apoptosis (9). Previously, we have demonstrated that DYRK2 phosphorylates p53 at Ser46 under severe DNA damage (10, 11). We also found that DYRK2 is activated by ataxia-telangiectasia mutated (ATM), which senses DNA damage, and triggers apoptotic cell death (12). If Ser46 phosphorylation could be induced by chemical compounds, the compounds might enable tumor cells to induce cell death. Therefore, Ser46 phosphorylation could be a molecular target for cancer therapy. Recent study demonstrated that Ser46 phosphorylation-dependent apoptosis is also induced by mutant huntingtin (mHtt) (13). Because the mHtt elicits ROS reproduction and mitochondria dysfunction, DNA damage response is constitutively activated in the mHtt-expressing cells. Thus, Ser46 phosphorylation is widely linked in human disease development. However, it is unclear how Ser46-phosphorylated p53 induces cell death.

Here, we report that AREG is identified as a Ser46 phosphorylation responsible gene by the microarray analysis. AREG interacts with DEAD-box RNA helicase p68 (DDX5) to regulate precursor microRNA processing. In this regard, Ser46-phosphorylated p53

Significance

The tumor suppressive function of p53 is tightly regulated by its posttranslational modifications. Although Ser46 phosphorylation is a critical modification for apoptosis induction, a molecular mechanism by which Ser46-phosphorylated p53 induces apoptosis remains unclear. Here, we clarify that amphiregulin (AREG) is specifically induced in a Ser46 phosphorylation-specific manner. Notably, AREG colocalizes with DEAD-box RNA helicase p68 (DDX5) in the nucleus and regulates tumor suppressive microRNA biogenesis in response to DNA damage. These findings support a model in which Ser46-phosphorylated p53 orchestrates tumor suppressive microRNA expression in the apoptotic response to DNA damage.

Author contributions: N.T. and K.Y. designed research; N.T., T.Y., J.K., Z.-G.L., and M.O. performed research; S.F. and S.H. contributed new reagents/analytic tools; N.T. and K.Y. analyzed data; and N.T. and K.Y. wrote the paper.

The authors declare no conflict of interest.

This article is a PNAS Direct Submission. M.O. is a guest editor invited by the Editorial Board.

Data deposition: The complete expression datasets have been deposited in the Array Express database, www.ebi.ac.uk/arrayexpress (accession no. E-MEXP-2556).

[1]To whom correspondence should be addressed. E-mail: kyoshida@jikei.ac.jp.

This article contains supporting information online at www.pnas.org/lookup/suppl/doi:10.1073/pnas.1313675111/-/DCSupplemental.

facilitates tumor suppressive miRNA maturation via AREG, leading to apoptotic cell death.

Results

Identification of AREG as a Direct Target of Phosphorylated p53 at Ser46. In an attempt to isolate target genes of p53 that are especially phosphorylated at Ser46, p53-deficient H1299 lung adenocarcinoma cells or SaOS-2 osteosarcoma cells were transfected with Flag vector, Flag-p53 wild type (WT), or the Flag-p53 mutant in which Ser46 was replaced by Ala (S46A). As shown previously, ectopic expression of p53-WT in p53-deficient cells was sufficient for induction of Ser46 phosphorylation (14). We obtained similar convincing evidence for Ser46 phosphorylation with p53-WT, but not p53-S46A (Fig. S1*A*). To explore target genes that depend on Ser46 phosphorylation, we purified mRNA from these transfected cells to apply the microarray analysis. Whereas ~54,000 probe sets were analyzed, to isolate p53 target genes, we compared gene expression profiles in p53-WT–transfected cells with those in the empty vector-transfected cells. As targets for p53, 793 or 1,804 probes, which were more than 1.5-fold increase, were chosen in H1299 or SaOS-2 cells, respectively. To further screen out target genes induced by phosphorylated p53 at Ser46, the expression profiles in p53-WT–transfected cells were compared with those in the p53-S46A transfectant. As targets for phosphorylated p53 at Ser46, 11 or 28 probes, which were more than a 1.5-fold increase, were chosen in H1299 or SaOS-2 cells, respectively. Eventually, one probe has been selected, which conforms the criteria for the transcriptional elevation, in a Ser46 phosphorylation-dependent manner in both cell lines (Fig. 1*A*). Surprisingly, the probe was coded for AREG that is known as a member of EGF. Analysis of microarray data indicated that induction of AREG mRNA in p53-WT is significantly higher than that in p53-S46A (Fig. 1*A*). To verify this finding, we performed real-time RT-PCR and semiquantitative RT-PCR. In concert with the microarray data, expression of p53-WT markedly increased AREG mRNA in H1299 cells (Fig. 1*B* and Fig. S1*B*). Moreover, in comparison with transfection with p53-WT, induction of AREG expression was diminished in cells transfected with p53-S46A (Fig. 1*B* and Fig. S1*B*). Taken together, these findings demonstrated that the transcription of AREG is upregulated by Ser46-phosphorylated p53. To further examine AREG expression in protein levels, H1299 cells were transfected with p53, then cell lysates were analyzed by Western blotting. In accordance with mRNA levels, AREG protein was highly inducible in cells transfected with p53-WT (Fig. 1*C*). By contrast, introduction of p53-S46A was little, if any, effect on inducible AREG expression (Fig. 1*C*), suggesting its dependency on Ser46 phosphorylation in protein levels.

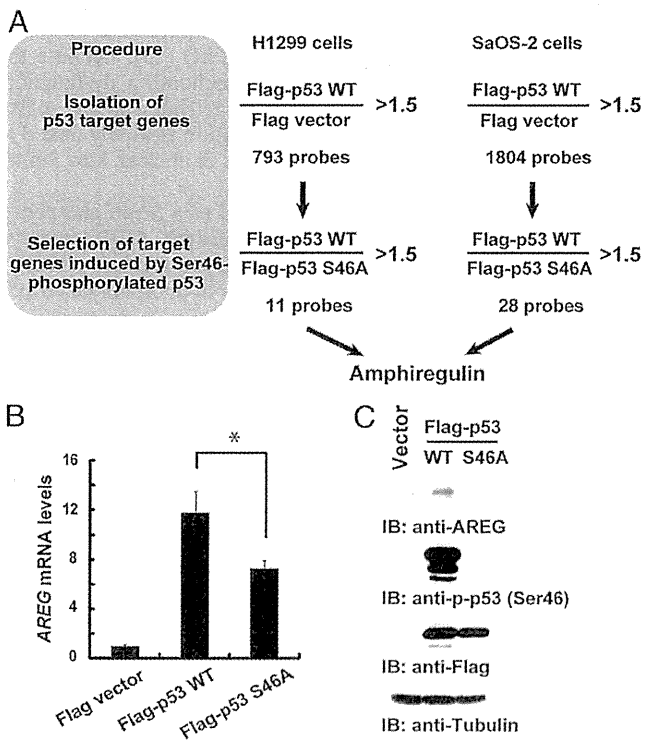

Fig. 1. Identification of target genes that are induced in a Ser46 phosphorylation-specific manner. (*A*) Numbers of GeneChip probes that are more than 1.5-fold up-regulated by Flag-p53 WT overexpression, compared with Flag vector and Flag-p53 S46A mutant expressing cells. AREG was identified by microarray analysis from both H1299 and SaOS-2 cells. (*B*) H1299 cells were transfected with Flag-vector, Flag-p53 WT, or the S46A mutant. Total RNA was analyzed by semiquantitative real-time PCR. $*P < 0.05$. (*C*) H1299 cells were transfected with Flag-vector, Flag-p53 WT, or the S46A mutant. Cell lysates were subjected to immunoblot analysis with anti-AREG, anti-phospho-p53 (Ser46) [p-p53 (Ser46)], anti-Flag, or anti-tubulin.

p53 Binds to and Transactivates the AREG Promoter. To define the potential p53-responsive elements in the AREG promoter, we searched the consensus p53-binding site (15) and found two matches for this sequence within 500 bp of the AREG initiation codon (Fig. 2*A*). To confirm that p53 binds to these elements in vivo, we performed chromatin immunoprecipitation (ChIP) assays. Chromatin was isolated from H1299 cells transfected with Flag vector, Flag-p53-WT, or Flag-p53-S46A and was immunoprecipitated with an anti-Flag antibody. Immunoprecipitated DNA was then analyzed by PCR with primers amplifying the AREG promoter region encompassing the putative p53-binding consensus elements (p53-CE; −561 to −361). The elements were specifically immunoprecipitated with anti-Flag in p53-WT–transduced cells, suggesting that p53 actually binds to AREG promoter in vivo (Fig. 2*B*). Moreover, there was no remarkable occupancy of p53-S46A on the p53-CE of AREG promoter (Fig. 2*B*), indicating that Ser46 phosphorylation is prerequisite for recruitment of p53 to the AREG promoter. To extend this finding in the physiological condition, human osteosarcoma U2OS cells were left untreated or treated with adriamycin (ADR). The analysis of ChIP showed that there was little immunoprecipitation of DNA fragments containing p53-CE in unstimulated cells (Fig. 2*C*). By contrast, occupancy of the AREG promoter by p53 was markedly increased after ADR stimulation (Fig. 2*C*). As a control, there was no detectable p53 occupancy of a control region (CR; −853 to −695) in the AREG promoter upstream to the p53-CE (Fig. 2*C*). Importantly, there was little, if any, p53 occupancy in cells pretreated with pofitherin-α, a specific p53 inhibitor (Fig. 2*C*). Previous study showed that DYRK2 is responsible for Ser46 phosphorylation in response to DNA damage (10). In this context, the demonstration that there was also little, if any, immunoprecipitates of p53-CE by silencing DYRK2 supports a model in which Ser46 phosphorylation triggers the p53 occupancy of AREG promoter (Fig. 2*C*).

To further prove the role of Ser46 phosphorylation for the promoter binding, we performed ChIP analysis with the anti-phospho-p53 (Ser46) antibody. Initially, we validated whether this antibody is useful for the immunoprecipitation. The results demonstrated that endogenous phosphorylated p53 is successfully immunoprecipitated with the antibody in nonsilencing siRNA (control siRNA)-transfected cells after DNA damage (Fig. S2*A*). Notably, in the absence of DYRK2, there was little, if any, immunoprecipitation of p53 (Fig. S2*A*), indicating that the phospho-Ser46–specific antibody is applicable for immunoprecipitation with high specificity. To verify the result, we monitored the endogenous phosphorylation levels of p53 (Fig. S2*B*). As shown previously, phosphorylation of p53 at Ser46 was abrogated

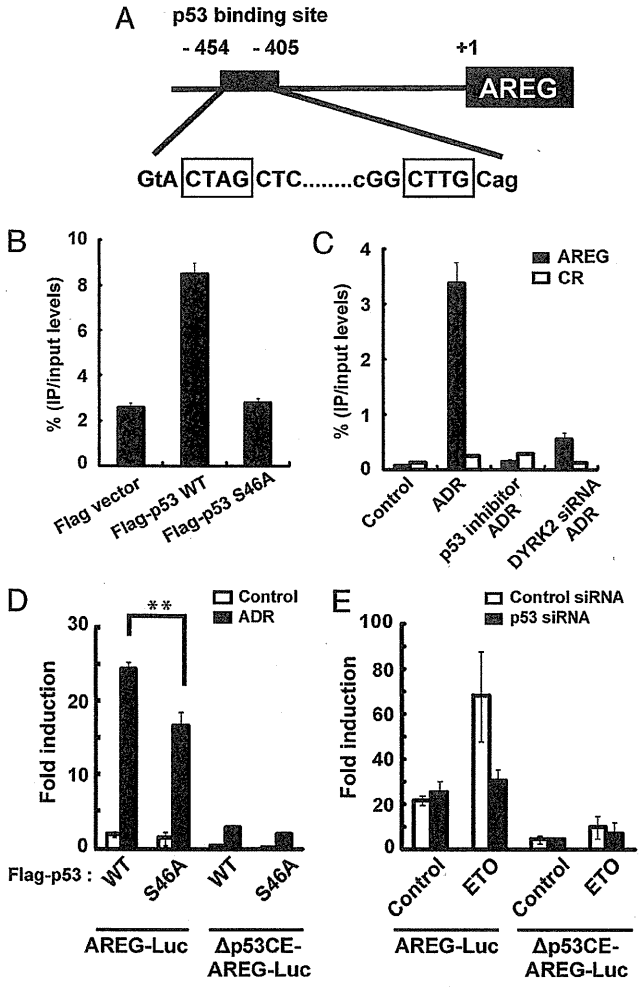

Fig. 2. AREG is a direct target gene of p53. (*A*) Schematic diagram of AREG promoter and p53 consensus motif. Capital letters indicate nucleotides that match the p53 consensus sequence. (*B*) H1299 cells were transfected with Flag-vector, Flag-p53 WT, or the S46A mutant. For ChIP assay, chromatin–protein complexes were immunoprecipitated with anti-Flag. Precipitated chromatin fragments were amplified by PCR with specific primers for p53-CE in the AREG promoter. (*C*) U2OS cells were transfected with nonsilencing siRNA (control siRNA) or DYRK2-specific siRNA, and then left untreated or treated with ADR and/or p53 inhibitor. Chromatin–protein complexes were immunoprecipitated with normal mouse IgG or anti-p53. Real-time PCR amplification was performed to analyze the chromatin-immunoprecipitated fragments by using primers that are designed for AREG promoter (AREG), or the outside of AREG promoter control region (CR). The data were normalized with the level of input control. (*D*) H1299 cells were cotransfected with pGL3 vector, AREG-Luc, or Δp53CE-AREG-Luc and Flag-p53 WT or the S46A mutant, and then treated with 0.5 μg/mL ADR for 24 h. The relative increase in luciferase activity was compared with cells transfected with pGL3 vector. $^{**}P < 0.01$. (*E*) U2OS cells were transfected with the reporter vectors and the control siRNA or p53-specific siRNA, and then treated with 10 μM ETO for 24 h. Luciferase assays were performed as described above.

in DYRK2 knockdown cells. Based on these findings, we performed ChIP analysis with this antibody. The results showed that phosphorylated p53 is recruited to the AREG promoter under genotoxic stress. By contrast, the recruitment was diminished by knocking down DYRK2 (Fig. S2*C*). These results strengthen the evidence that phosphorylated p53 at Ser46 is specifically recruited to the AREG promoter in response to DNA damage.

To establish whether p53 binding is functionally relevant, we investigated the p53-CE in the AREG promoter for the ability to drive a luciferase reporter gene (AREG-Luc) in response to cotransfection of p53 into H1299 cells (Fig. 2*D*). In concert with findings obtained from ChIP analysis, upon exposure to ADR, the luciferase activity was significantly up-regulated in cells transduced with p53 WT (Fig. 2*D*). By contrast, ectopic expression of p53-S46A attenuated ADR-induced luciferase activity in comparison with that of p53-WT (Fig. 2*D*). Deletion of p53-CE in AREG-Luc (Δp53CE-AREG-Luc) completely abrogated the luciferase activity in p53-WT–transfected cells after DNA damage (Fig. 2*D*). Identical effects were obtained in p53-S46A–transfected cells (Fig. 2*D*). To confirm that endogenous p53 plays a role in the induction of AREG by DNA damage, U2OS cells were transfected with AREG-Luc or Δp53CE-AREG-Luc followed by treatment with etoposide (ETO). As found in transfected H1299 cells, DNA damage enhanced the luciferase activity, whereas the absence of p53-CE completely impaired its induction (Fig. 2*E*). Significantly, silencing p53 conferred resistance to the augment of ETO-induced luciferase activity regardless of the presence or absence of p53-CE (Fig. 2*E*). Taken together, these findings indicated that p53 transactivates AREG via p53-CE on the AREG promoter in response to DNA damage.

p53 Induces AREG in Response to DNA Damage. To determine whether p53 physiologically induces AREG expression after genotoxic stress, U2OS cells were transfected with a control siRNA or a siRNA targeting for p53 (p53 siRNA) followed by treatment with ADR. Analysis of real-time RT-PCR revealed that upon exposure of cells to ADR, AREG mRNA was increased at relatively later periods (Fig. 3*A*), which specifically coincided with the level of Ser46 phosphorylation (14). Importantly, abrogation of p53 expression completely suppressed increment of AREG mRNA after ADR treatment (Fig. 3*A*), indicating that DNA damage-induced augment of AREG mRNA requires p53. To extend these findings in protein levels, U2OS cells were transfected with the control siRNA, or the p53 siRNA followed by ADR exposure. As shown for the mRNA levels, the expression of AREG was elevated at 24 h in mock-transfected U2OS cells (Fig. S3), indicating relatively later-phase induction similar to Ser46 phosphorylation. In sharp contrast, there was no detectable AREG expression in cells silenced for p53 (Fig. S3). These results demonstrated that AREG is a target of p53 in response to DNA damage. Given that Ser46-phosphorylated p53 is recruited to the AREG promoter (Fig. 2 *B* and *D*), we assessed whether AREG expression coincides with the Ser46 phosphorylation level. AREG was detectable at 24 h after ADR exposure in accordance with Ser46 phosphorylation (Fig. 3*B*). However, in DYRK2 knockdown cells, AREG expression was not up-regulated by DNA damage (Fig. 3*B* and Fig. S2*B*). Importantly, DNA damage-induced Ser46 phosphorylation was markedly attenuated in DYRK2 knockdown cells. Taken together, AREG is induced by p53 in a Ser46 phosphorylation-specific manner.

Accumulating lines of evidence show that AREG is transported to the plasma membrane and is secreted to act as a ligand for EGFR (16). However, recent study demonstrated that intracellular AREG translocates to the inner nuclear envelope and then regulates chromatin remodeling (7). These reports thus suggest that AREG function is diverse, which is determined by its cellular localization. Given that AREG is shedded by ADAM17 on the cell surface and secreted from cells, we measured the AREG levels in the cell culture media. Of note, AREG was initially discovered in MCF-7 cells (17). As reported previously, AREG was released to extracellular fluid in response to TPA stimulation in MCF-7 cells (Fig. 3*C*). In contrast, AREG production was attenuated by cotreatment with ADAM17 inhibitor, TAPI. Importantly, there was little, if any, increase AREG production in response to various DNA damage stimuli. Furthermore, in U2OS cells, AREG production levels were

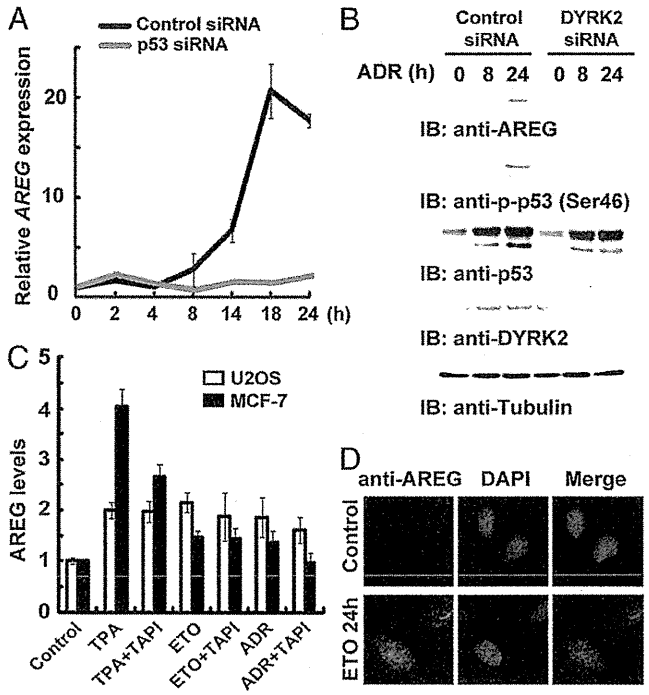

Fig. 3. AREG is induced by p53 in response to DNA damage. (*A*) U2OS cells were transfected with control siRNA or p53 siRNA to reduce endogenous p53 expression. At 48 h after transfection, cells were left untreated or treated with ADR for the indicated times. Total RNA was analyzed by semi-quantitative real-time PCR. (*B*) U2OS cells were transfected with control siRNA or DYRK2 siRNA and then treated with ADR for the indicated times. Cell lysates were subjected to immunoblot analysis with the indicated antibodies. (*C*) MCF-7 and U2OS cells were treated with 100 nM TPA, 10 μM TAPI, 2 μg/mL ADR, or 20 μM ETO for 24 h. The amount of secreted AREG in the culture medium was measured by ELISA. The data were normalized to values from each untreated cells. The results are represented as mean ± SD obtained from triplicate ELISA values. (*D*) U2OS cells were treated with 10 μM ETO for 24 h. Cells were immunostained with anti-AREG (FITC). The nuclei were detected with DAPI.

remained unchanged even after treatment with TPA or genotoxin (Fig. 3*C*). These data indicated that AREG is independent from the shedding by ADAM17 in the DNA damage response. To examine where AREG localizes under DNA damage condition, U2OS cells were immunostained with anti-AREG antibody (Fig. 3*D*). As similarly shown for Western blotting (Fig. 3*B*), AREG expression was increased after DNA damage. Notably, AREG was not expressed in the plasma membrane, but predominantly localized in the nucleus upon ETO treatment (Fig. 3*D*). Collectively, these results suggest that AREG is induced by p53 and is targeted to the nucleus in response to DNA damage.

AREG Interacts with DDX5 and Drosha. To characterize nuclear function of AREG, we intended to identify AREG-associated protein by mass spectrometry. U2OS cells were transfected with YFP-vector or YFP-tagged AREG, and cell lysates were immunoprecipitated with anti-GFP antibody. Immune complexes were analyzed by 2-Dimensional Image Converted Analysis of Liquid (2DICAL) chromatography and mass spectrometry (18). By 2DICAL analysis, the 79 peaks were statistically significant between the immunoprecipitates from AREG-YFP and YFP ($P < 0.05$). The MS peaks were subjected to MS/MS analysis to identify amino acid sequences (Table S1). Mascot search showed that DDX5 was identified as an AREG binding protein (Fig. S4 *A* and *B*). The MS peak of immunoprecipitated AREG was detected by these analyses (Fig. S4 *C* and *D*). To confirm this finding, U2OS cells were transfected with YFP-vector or AREG-YFP followed by immunoprecipitation with anti-GFP antibody. The analysis with anti-DDX5 revealed that AREG was interacted with DDX5 in cells (Fig. S5). To extend this finding, DDX5 was immunoprecipitated in the presence or absence of ETO. The results demonstrated that endogenous DDX5 interacts with AREG upon genotoxic stimuli (Fig. 4*A*, *Left*). Given that DDX5 is one of the components of Drosha complex, we determined whether Drosha also interacts with AREG. Endogenous Drosha was immunoprecipitated with anti-Drosha followed by immunoblot analysis with anti-AREG antibody. The results demonstrated that endogenous Drosha interacts with AREG in the presence of ETO (Fig. 4*A*, *Center*). These results support our model in which AREG modulates the microRNA processing with DDX5–Drosha complex. To clarify subcellular localization of DDX5 following DNA damage, U2OS cells were immunostained with anti-DDX5 and anti-AREG antibodies. As shown previously, AREG localized in the nucleus under the DNA-damaged condition (Fig. 3*D*). In this circumstance, DDX5 colocalized with AREG in the nucleus (Fig. 4*B*). Taken together, these findings demonstrate that nuclear AREG interacts with DDX5 upon genotoxic stress.

AREG Regulates microRNA Processing To Induce Apoptosis. Previous study has shown that DDX5 engages microRNA processing, especially among the converting step from primary microRNA (miRNAs) to precursor miRNA (19). DDX5 regulates miRNAs (i.e., miR-15a) biogenesis in response to DNA damage. In addition, because Ser46 phosphorylation is an indispensable modification for p53-dependent apoptosis, it is plausible that AREG exerts induction of apoptosis. Based on these findings, we hypothesized that AREG regulates tumor suppressive miRNAs processing via DDX5 interaction. To address this possibility,

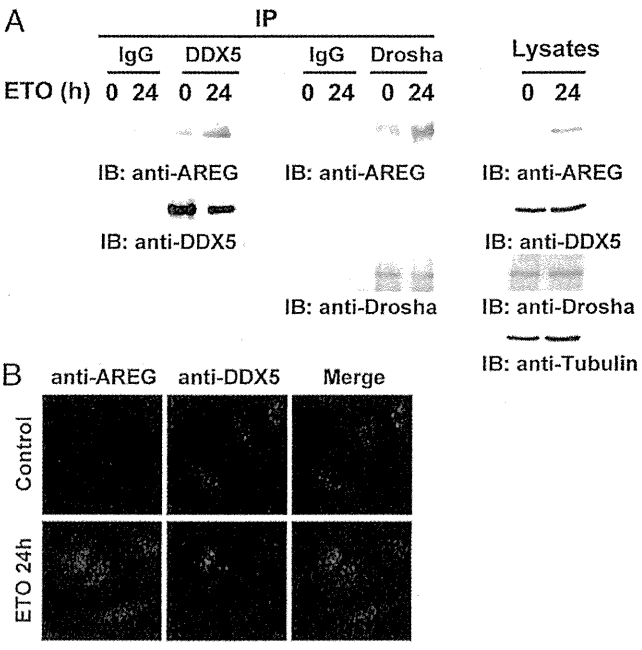

Fig. 4. AREG associates with DDX5 with Drosha. (*A*) U2OS cells were treated with 10 μM ETO for 24 h. Lysates were immunoprecipitated with normal mouse IgG, anti-DDX5, or anti-Drosha followed by immunoblot analysis with indicated antibodies. Cell lysates were also analyzed by Western blotting. (*B*) U2OS cells were treated with 10 μM ETO for 24 h. Cells were immunostained with anti-AREG (FITC) and anti-DDX5 (rhodamine). The nuclei were detected with DAPI.

precursor miRNA was isolated from U2OS cells and then analyzed by real-time PCR. As shown by Suzuki et al. (19), pre-miR-15a was increased by DNA damage, whereas pri-miR-15a levels remained unchanged (Fig. 5 *A* and *B*). This data thus confirmed that miR-15a expression is posttranscriptionally regulated. In AREG knockdown cells, pre-miR-15a levels were significantly reduced, indicating that AREG modulates miR-15a processing (Fig. 5*B*). Because a major target of the miR-15a is antiapoptotic protein Bcl-2 (20), we examined Bcl-2 expression under the same conditions (Fig. 5*C*). Bcl-2 expression was declined upon severe DNA damage. By contrast, the decrease was little, if any, observed in AREG knockdown cells. This finding indicates that AREG regulates Bcl-2 expression through processing of miR-15a. To assess whether endogenous AREG is involved in apoptosis induction, U2OS cells were transfected with the control siRNA or the AREG siRNA followed by treatment with ADR. Silencing AREG significantly attenuated apoptosis elicited by ADR (Fig. 5*D*). To further investigate whether AREG regulates apoptosis induction via the miRNA biogenesis, miR-15a inhibitor was cotransfected with control siRNA or AREG siRNA. In the control siRNA-transfected U2OS cells, DNA damage-induced apoptosis was remarkably suppressed in the presence of miR-15a inhibitor (Fig. 5*D*). This result supported that miR-15a is a prerequisite miRNA for apoptosis induction. In contrast, apoptosis induction was not attenuated by AREG depletion regardless of miR-15a inhibitor transfection, suggesting that AREG induces apoptosis via miR-15 induction (Fig. 5*D*).

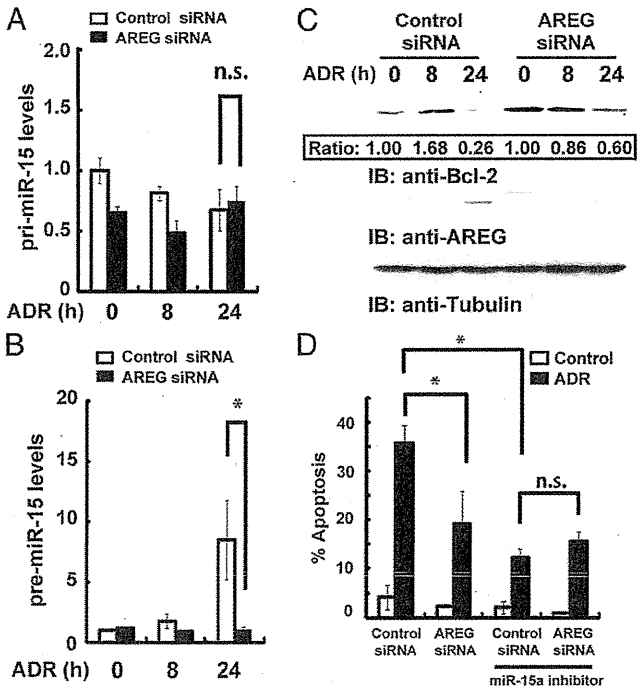

Fig. 5. AREG induces apoptosis in response to DNA damage. (*A* and *B*) U2OS cells were transfected with control or AREG-specific siRNA and then treated with ADR for the indicated times. Total RNA was amplified with pri-miR-15a specific primers (*A*) or pre-miR-15a–specific primers (*B*). Data represent mean ± SD of relative induction. n.s., not significant; $*P < 0.05$. (*C*) U2OS cells were transfected with control siRNA or AREG siRNA and treated with ADR for indicated times. Cell lysates were analyzed by Western blotting with indicated antibodies. Relative band intensity (anti-Bcl-2) is shown. (*D*) U2OS cells were transfected with control siRNA, AREG siRNA, or miR-15a inhibitor and then treated with ADR for 24 h. Apoptotic cells were quantified by TUNEL assays. Data represent the mean ± SD: n.s., not significant; $*P < 0.05$.

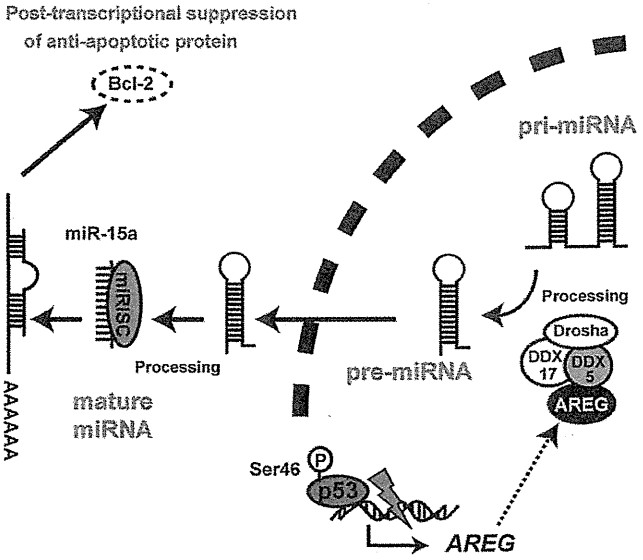

Fig. 6. The model of AREG-mediated apoptosis regulation. In response to DNA damage, AREG is induced by p53 and interacts with DDX5 and Drosha. The AREG complex contributes to biogenesis of DNA damage-induced microRNAs including miR-15a that targets antiapoptotic factor Bcl-2. AREG regulates apoptosis induction via the microRNA processing.

To examine whether AREG modulates the microRNA biogenesis besides miR-15a, the expression levels of other precursor miRNAs were monitored by real-time PCR. Given that miR-34 is one target for p53 in response to DNA damage (21), we analyzed pri-miR-34 expression in U2OS cells. As shown previously, pri-miR-34 expression increased following genotoxic stimuli. In AREG-silencing cells, pri-miR-34 expression was induced at a comparable level to that in control siRNA-transfected cells. This finding demonstrated that miR-34 transcription is induced by DNA damage, which is independent of AREG (Fig. S6*A*). Pri-miR-143 expression remained unchanged after ADR treatment in both transfectants (Fig. S6*B*). These results suggest that AREG is not involved in microRNA transcription. We further examined expression levels of pre-miR-34 and pre-miR-143 under the same experimental conditions. They were increased by DNA damage. By contrast, in AREG knockdown cells, they were markedly attenuated, suggesting that AREG regulates the processing of miR-34 and miR-143 (Fig. S6 *C* and *D*). Taken together, these findings indicate that AREG contributes to the miRNA biogenesis, not only in miR-15, but also other miRNAs.

We also examined whether DDX5 or DDX17 modulates AREG-mediated apoptotic cell death. U2OS cells were cotransfected with AREG siRNA and DDX5 siRNA or DDX17 siRNA. Apoptosis induction was monitored by TUNEL assay. As previously shown (Fig. 5*D*), AREG knockdown was associated with the attenuation of apoptotic cell death compared with the control siRNA transfection (Fig. S7). Importantly, additional knockdown of DDX5 or DDX17 had no further effect on apoptosis induction (Fig. S7). These results suggest that AREG is essential for the process of precursor microRNAs involved in apoptosis regulation.

Taken together, these findings demonstrated that AREG induces apoptosis in response to genotoxic insult by modulating the microRNA processing within the Drosha complex (Fig. 6).

Discussion

Tumor suppressor p53 has a great variety of function to prevent tumor progression. Especially, apoptotic induction is an effective

CELL BIOLOGY

mechanism for tumor elimination. Despite phosphorylation of p53 at Ser46 that dramatically induces apoptosis, how phosphorylated p53 induces apoptosis remains unclear. To identify Ser46 phosphorylation-responsible genes, gene expression profiles from p53 WT cells were compared with those from S46A mutant. We successfully identified AREG as a phospho-Ser46 responsible gene. Notably, Ser46 phosphorylation allows p53 to target the AREG promoter. Given that Ser46-phosphorylated p53 induces the expression of p53AIP1 that promotes apoptosis (14), Ser46 phosphorylation changes promoter affinity of p53 to the promoters with proapoptotic genes.

Recent studies demonstrated the function of p53 in the microRNA biogenesis. miR-34 was originally identified as a microRNA that is directly transactivated by p53 (21, 22). Suzuki et al. showed that p53 facilitates microRNA processing with Drosha (19). Thus, p53 directly regulates microRNA expression at both transcriptional and posttranscriptional levels. The present study shows that p53 engages microRNA production via AREG, which is a target for p53, indicating that p53 indirectly modulates the microRNA biogenesis. In this context, p53 modified the microRNA biogenesis in the various steps. In response to DNA double-strand break, ATM phosphorylates downstream effectors to transduce the damage signal. ATM regulates the microRNA biogenesis via KSRP phosphorylation (23). Taken together, these tumor suppressive factors regulate the microRNA biogenesis, suggesting that dysregulation of microRNA metabolism is observed in tumors. Accumulating evidence has demonstrated that microRNA levels are decreased in tumors (24), and that defects in microRNA processing are observed in tumor (25). In these regards, posttranscriptional regulation for the microRNA biogenesis is fundamental for tumor inhibition. We reported that DYRK2-depleted cells contribute to tumorigenesis in vivo (26, 27). In the current study, AREG expression remained little, if any, detectable in the DYRK2 knockdown cells. Loss of AREG could not suppress Bcl-2 expression under severe DNA damage mainly due to the failure of pri-miR-15a processing. In this context, the defect in the microRNA biogenesis might accelerate tumorigenesis.

AREG was originally identified in MCF7 cells treated with TPA. Furthermore, AREG is well known as a bifunctional protein for cell growth (17). Initially, AREG is synthesized as a precursor protein, and the precursor is transported to the plasma membrane and proteolytically cleaved by ADAM17 (28). Cleaved AREG binds to EGFR to facilitate receptor phosphorylation. Thus, secreted AREG functions as a ligand to promote proliferation. In contrast, other reports suggested that AREG has a tumor inhibitory function (2, 17). Intriguingly, AREG translocates to the inner nuclear membrane to induce heterochromatinization, thereby suppressing transcription (7). In ovarian cells, AREG localizes in the nucleus (5, 6); however, nuclear function of AREG has remained to be elucidated. In the present study, we clarified that nuclear AREG modulates tumor suppressive miRNA expression via microRNA processing to inhibit tumor growth. AREG possesses two nuclear localization sequences; however, machinery of nuclear trafficking of AREG is not fully understood. Elucidation of the regulation for intracellular localization of AREG is requisite for characteristics of its function.

Materials and Methods

Experimental details are described in *SI Materials and Methods*. All results are expressed as mean values ± SD of at least three independent experiments. Unpaired Student *t* test was used to generate statistical analysis. All microarray data (29) have been deposited in the ArrayExpress database under accession no. E-MEXP-2556.

ACKNOWLEDGMENTS. We thank Ayako Igarashi for technical assistance. This work was supported by grants from the Ministry of Education, Science and Culture of Japan, the Jikei University Graduate Research Fund, the NOVARTIS Foundation for the Promotion of Science, Suzuken Memorial Foundation, Uehara Memorial Foundation, the Astellas Foundation for Research on Medical Resources, Takeda Science Foundation, the Mochida Memorial Foundation for Medical and Pharmaceutical Research, the Sumitomo Foundation, the Naito Foundation, Japan Foundation for Applied Enzymology, Project Mirai Cancer Research Grants, the Yasuda Memorial Foundation, the Japan Society for the Promotion of Science, and the Nakajima Foundation.

1. Sahin U, et al. (2004) Distinct roles for ADAM10 and ADAM17 in ectodomain shedding of six EGFR ligands. *J Cell Biol* 164(5):769–779.
2. Plowman GD, et al. (1990) The amphiregulin gene encodes a novel epidermal growth factor-related protein with tumor-inhibitory activity. *Mol Cell Biol* 10(5):1969–1981.
3. Brown CL, Meise KS, Plowman GD, Coffey RJ, Dempsey PJ (1998) Cell surface ectodomain cleavage of human amphiregulin precursor is sensitive to a metalloprotease inhibitor. Release of a predominant N-glycosylated 43-kDa soluble form. *J Biol Chem* 273(27):17258–17268.
4. Neelam B, et al. (1998) Structure-function studies of ligand-induced epidermal growth factor receptor dimerization. *Biochemistry* 37(14):4884–4891.
5. Modrell B, McDonald VL, Shoyab M (1992) The interaction of amphiregulin with nuclei and putative nuclear localization sequence binding proteins. *Growth Factors* 7(4):305–314.
6. Johnson GR, et al. (1991) Response to and expression of amphiregulin by ovarian carcinoma and normal ovarian surface epithelial cells: Nuclear localization of endogenous amphiregulin. *Biochem Biophys Res Commun* 180(2):481–488.
7. Isokane M, et al. (2008) Plasma-membrane-anchored growth factor pro-amphiregulin binds A-type lamin and regulates global transcription. *J Cell Sci* 121(Pt 21):3608–3618.
8. Yoshida K (2008) Nuclear trafficking of pro-apoptotic kinases in response to DNA damage. *Trends Mol Med* 14(7):305–313.
9. Taira N, Yoshida K (2012) Post-translational modifications of p53 tumor suppressor: Determinants of its functional targets. *Histol Histopathol* 27(4):437–443.
10. Taira N, Nihira K, Yamaguchi T, Miki Y, Yoshida K (2007) DYRK2 is targeted to the nucleus and controls p53 via Ser46 phosphorylation in the apoptotic response to DNA damage. *Mol Cell* 25(5):725–738.
11. Yoshida K (2008) Role for DYRK family kinases on regulation of apoptosis. *Biochem Pharmacol* 76(11):1389–1394.
12. Taira N, Yamamoto H, Yamaguchi T, Miki Y, Yoshida K (2010) ATM augments nuclear stabilization of DYRK2 by inhibiting MDM2 in the apoptotic response to DNA damage. *J Biol Chem* 285(7):4909–4919.
13. Grison A, et al. (2011) Ser46 phosphorylation and prolyl-isomerase Pin1-mediated isomerization of p53 are key events in p53-dependent apoptosis induced by mutant huntingtin. *Proc Natl Acad Sci USA* 108(44):17979–17984.
14. Oda K, et al. (2000) p53AIP1, a potential mediator of p53-dependent apoptosis, and its regulation by Ser-46-phosphorylated p53. *Cell* 102(6):849–862.
15. el-Deiry WS, Kern SE, Pietenpol JA, Kinzler KW, Vogelstein B (1992) Definition of a consensus binding site for p53. *Nat Genet* 1(1):45–49.
16. Busser B, Sancey L, Brambilla E, Coll JL, Hurbin A (2011) The multiple roles of amphiregulin in human cancer. *Biochim Biophys Acta* 1816(2):119–131.
17. Shoyab M, McDonald VL, Bradley JG, Todaro GJ (1988) Amphiregulin: a bifunctional growth-modulating glycoprotein produced by the phorbol 12-myristate 13-acetate-treated human breast adenocarcinoma cell line MCF-7. *Proc Natl Acad Sci USA* 85(17):6528–6532.
18. Ono M, et al. (2006) Label-free quantitative proteomics using large peptide data sets generated by nanoflow liquid chromatography and mass spectrometry. *Mol Cell Proteomics* 5(7):1338–1347.
19. Suzuki HI, et al. (2009) Modulation of microRNA processing by p53. *Nature* 460(7254):529–533.
20. Cimmino A, et al. (2005) miR-15 and miR-16 induce apoptosis by targeting BCL2. *Proc Natl Acad Sci USA* 102(39):13944–13949.
21. Chang TC, et al. (2007) Transactivation of miR-34a by p53 broadly influences gene expression and promotes apoptosis. *Mol Cell* 26(5):745–752.
22. Raver-Shapira N, et al. (2007) Transcriptional activation of miR-34a contributes to p53-mediated apoptosis. *Mol Cell* 26(5):731–743.
23. Zhang X, Wan G, Berger FG, He X, Lu X (2011) The ATM kinase induces microRNA biogenesis in the DNA damage response. *Mol Cell* 41(4):371–383.
24. Lu J, et al. (2005) MicroRNA expression profiles classify human cancers. *Nature* 435(7043):834–838.
25. Thomson JM, et al. (2006) Extensive post-transcriptional regulation of microRNAs and its implications for cancer. *Genes Dev* 20(16):2202–2207.
26. Taira N, et al. (2012) DYRK2 priming phosphorylation of c-Jun and c-Myc modulates cell cycle progression in human cancer cells. *J Clin Invest* 122(3):859–872.
27. Mimoto R, et al. (2013) DYRK2 controls the epithelial-mesenchymal transition in breast cancer by degrading Snail. *Cancer Lett* 339(2):214–225.
28. Scheller J, Chalaris A, Garbers C, Rose-John S (2011) ADAM17: a molecular switch to control inflammation and tissue regeneration. *Trends Immunol* 32(8):380–387.
29. Kimura J, Kudoh T, Miki Y, Yoshida K (2011) Identification of dihydropyrimidinase-related protein 4 as a novel target of the p53 tumor suppressor in the apoptotic response to DNA damage. *Int J Cancer* 128(7):1524–1531.

Supporting Information

Taira et al. 10.1073/pnas.1313675111

SI Materials and Methods

Cell Culture. U2OS cells were cultured in RPMI medium 1640 supplemented with 10% (vol/vol) heat-inactivated FBS, 100 units/mL penicillin, and 100 mg/mL streptomycin. H1299 cells, SaOS-2 cells, and MCF-7 cells were grown in DMEM containing 10% FBS and supplements. Cells were treated with adriamycin (ADR; Sigma-Aldrich) or etoposide (ETO; Sigma-Aldrich).

Microarray Analysis. H1299 cells and SaOS-2 cells were transfected with Flag-tagged p53 wild type or S46A mutant. Total RNA were purified and used for microarray analysis by using the Human Genome U133 plus 2.0 array (Affymetrix) as described (1). The results from Genechip analysis are available at www.ebi.ac.uk/arrayexpress, under accession no. E-MEXP-2556.

Plasmid and siRNA. Human p53 was cloned into pcDNA3-FLAG vector (2). Alanine-substituted mutant of p53 was constructed by site-directed mutagenesis. Promoter region of amphiregulin (AREG) was cloned into the pGL3 basic vector. Human AREG was subcloned into the pEYFP vector (3). The control siRNA and DYRK2-, p53-, and AREG-specific siRNA were purchased from Qiagen and Invitrogen. Plasmids or siRNA were transfected by using FuGENE9 (Roche) or Lipofectamine RNAi MAX (Invitrogen), respectively. The miR-15a inhibitor was obtained from Ambion. The inhibitor was transfected by using Lipofectamene 2000 (Invitrogen).

Immunoblot, Immunoprecipitation, and Immunofluorescence Analyses. Cell lysates were prepared as described (4). Lysates were separated by SDS/PAGE and transferred to nitrocellulose membrane. The membranes were incubated with anti-phospho-p53 (Ser46) (Bioacademia), anti-p53 (Santa Cruz Biotechnology), anti-Flag (Sigma-Aldrich), anti-GFP (Nacalai tesque), anti-Bcl-2 (Zymed), anti-DYRK2 (Human Protein Atlas), anti-DEAD-box RNA helicase p68 (DDX5) (Millipore), anti-DDX17 (abcam), anti-Drosha (Santa Cruz Biotechnology), or anti-tubulin (Sigma-Aldrich). Polyclonal antibody to amino acids 233–250 of the human AREG was generated (5). Immune complexes were incubated with secondary antibodies and visualized by chemiluminescence (Perkin-Elmer). For immunoprecipitation, lysates were incubated with anti-GFP (MBL), anti-DDX5, or anti-Drosha for 2 h at 4 °C. Immune complexes were precipitated by protein G. For immunofluorescence, cells were left untreated or treated with ETO for 24 h. Cells were fixed in methanol for 5 min and permeabilized with 1% Triton X-100 for 15 min. After washing once with PBS, cells were blocked with goat serum in PBS for 1 h. After washing with PBS-T (0.05% Tween-20) three times, cells were incubated with anti-AREG and/or anti-DDX5. Immune complexes were then stained with a goat anti-rabbit secondary antibody-conjugated FITC or a goat anti-mouse secondary antibody-conjugated rhodamine. Nuclei were stained with DAPI (Vector Laboratories).

Densitometric Analysis. The band intensity was calculated by the densitometric analysis with the ImageJ program. The score was normalized by the signal intensity of nondamaged cells.

Semiquantitative Real-Time PCR. Precursor microRNA expression was analyzed by real-time PCR as described (6).

Reporter Assay. Luciferase activities were measured at 48 h after transfection by using the Bright-Glo Luciferase assay system (Promega) according to the manufacturer's protocol. The relative increase in activity compared with cells transfected with pGL3 vector was determined as described (7).

Chromatin Immunoprecipitation (ChIP) Assay. ChIP assay was performed as described (8). Immunoprecipitation was carried out with normal mouse IgG, anti-Flag, anti-p53, or anti-phospho-p53 (Ser46). Immunoprecipitated DNA fragments were amplified and subjected to semiquantitative RT-PCR. The data were normalized for the level of input control. The following primers were used for ChIP assays. For AREG promoter, 5′-gtacttttacatctaaatacgga-3′ and 5′-gtgcgtaaggattcgctgagaggaa-3′; Control region (CR), 5′-catatccacctggctttgaacat-3′ and 5′-ggccagaatttcaaatcccctcac-3′.

AREG Production. Cells were plated onto 96-well culture plate and treated with 12-*O*-tetradecanoylphorbol-13-acetate (TPA), TNF-alpha protease inhibitor (TAPI), ADR, or ETO for 24 h. The amount of secreted AERG was measured by using human amphiregulin DuoSet (R&D Systems) according to the manufacturer's protocol.

Mass Spectrometry Analysis. U2OS cells were transfected with YFP vector or YFP-tagged AREG. After 48 h, cells were harvested and cell lysates were immunoprecipitated with GFP antibody, and then binding proteins were eluted with 10% (vol/vol) sodium deoxycholate (SDC) solution. Samples were digested with sequencing grade modified trypsin (Promega) overnight. For LC-MS analysis, peptides were purified and resuspended with 0.1% formic acid. Acquired data from LC-MS were analyzed and quantified by using 2DICAL software (9).

Apoptosis Assay. Transiently transfected U2OS cells were cultured with poly-D-lysine–coated 4-well chamber slides. Apoptosis was detected by TUNEL assays by using DeadEnd Fluorometric TUNEL System (Promega). Statistical comparisons within the treatment groups were made by the Student *t* test. A P value of < 0.05 was considered to be statistically significant.

1. Kimura J, Kudoh T, Miki Y, Yoshida K (2011) Identification of dihydropyrimidinase-related protein 4 as a novel target of the p53 tumor suppressor in the apoptotic response to DNA damage. *Int J Cancer* 128(7):1524–1531.
2. Yoshida K, Liu H, Miki Y (2006) Protein kinase C delta regulates Ser46 phosphorylation of p53 tumor suppressor in the apoptotic response to DNA damage. *J Biol Chem* 281(9): 5734–5740.
3. Nakayama H, et al. (2012) Cell surface annexins regulate ADAM-mediated ectodomain shedding of proamphiregulin. *Mol Biol Cell* 23(10):1964–1975.
4. Taira N, Nihira K, Yamaguchi T, Miki Y, Yoshida K (2007) DYRK2 is targeted to the nucleus and controls p53 via Ser46 phosphorylation in the apoptotic response to DNA damage. *Mol Cell* 25(5):725–738.
5. Isokane M, et al. (2008) Plasma-membrane-anchored growth factor pro-amphiregulin binds A-type lamin and regulates global transcription. *J Cell Sci* 121(Pt 21):3608–3618.
6. Suzuki HI, et al. (2009) Modulation of microRNA processing by p53. *Nature* 460(7254): 529–533.
7. Liu H, Lu ZG, Miki Y, Yoshida K (2007) Protein kinase C delta induces transcription of the TP53 tumor suppressor gene by controlling death-promoting factor Btf in the apoptotic response to DNA damage. *Mol Cell Biol* 27(24):8480–8491.
8. Nihira K, et al. (2010) Pim-1 controls NF-kappaB signalling by stabilizing RelA/p65. *Cell Death Differ* 17(4):689–698.
9. Ono M, et al. (2006) Label-free quantitative proteomics using large peptide data sets generated by nanoflow liquid chromatography and mass spectrometry. *Mol Cell Proteomics* 5(7):1338–1347.

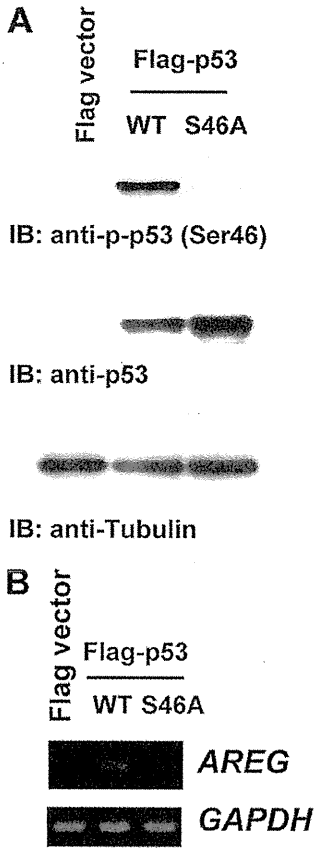

Fig. S1. AREG is induced by phosphorylated p53 at Ser46. (*A*) SaOS-2 cells were transfected with Flag-vector, Flag-p53 wild type, or the S46A mutant. Cell lysates were subjected to immunoblot analysis with indicated antibodies. (*B*) H1299 cells were transfected with Flag-vector, Flag-p53 WT, or the S46A mutant. Total RNA was analyzed by RT-PCR.

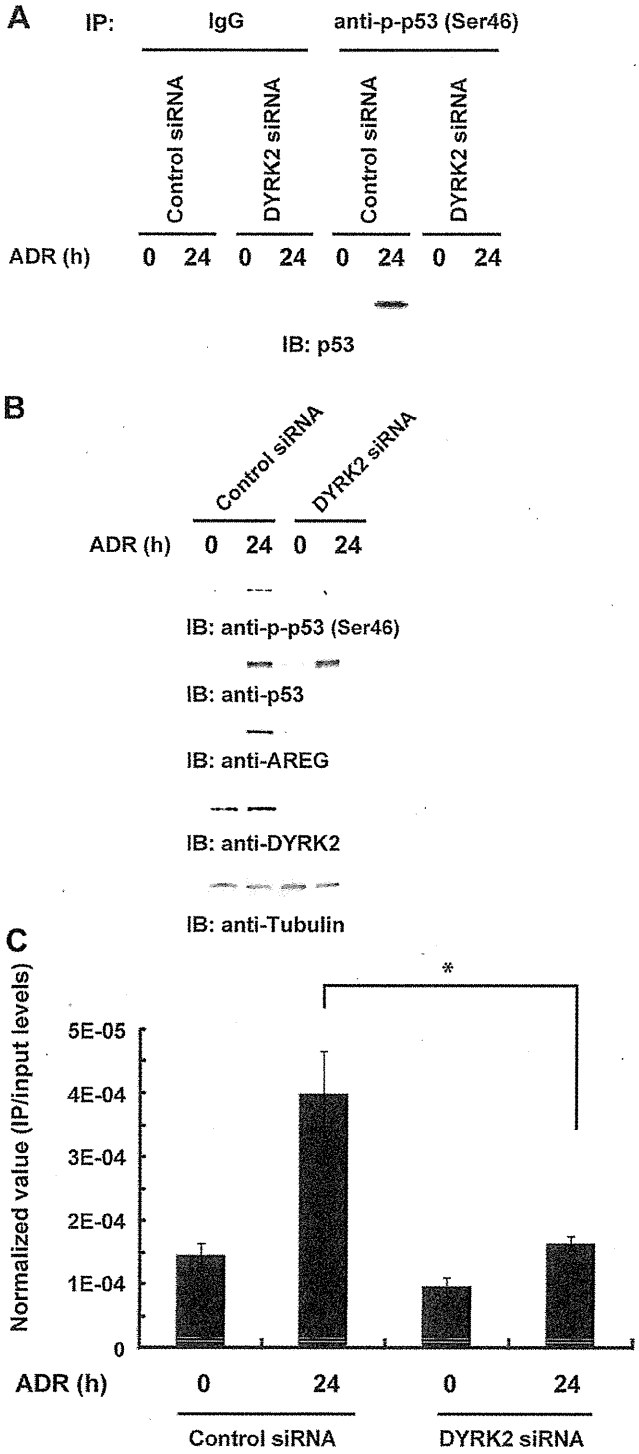

Fig. S2. Phosphorylated p53 selectively binds to AREG promoter. U2OS cells were transfected with nonsilencing siRNA (control siRNA) or DYRK2 siRNA, and then treated with ADR. (*A*) Lysates were immunoprecipitated with normal mouse IgG or anti–phospho-p53 (Ser46) [anti–p-p53 (Ser46)]. Immune complexes were subjected to immunoblot analysis with anti-p53. (*B*) Cell lysates were analyzed by Western blotting with indicated antibodies. (*C*) Chromatin–protein complexes were immunoprecipitated with anti–p-p53 (Ser46). Precipitated chromatin fragments were amplified by real-time PCR with specific primers for the AREG promoter. $*P < 0.05$.

Fig. S3. AREG is a physiological target gene for p53. U2OS cells were transfected with control siRNA or p53 siRNA and then treated with ADR for the indicated hours. Cell lysates were subjected to immunoblot with anti-AREG (*Top*), anti-p53 (*Middle*), or anti-tubulin (*Bottom*).

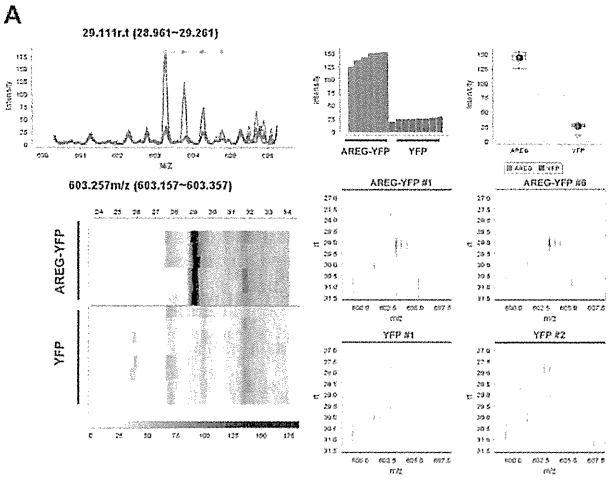

#	a	a**	a*	a***	b	b**	b*	b***	Seq.	y	y**	y*	y***	#
1	86.0964	43.5519			114.0913	57.5493			L					8
2	199.1805	100.0939			227.1754	114.0913			L	872.4836	436.7454	855.4571	428.2322	7
3	327.2391	164.1232	310.2125	155.6099	355.2340	178.1206	338.2074	169.6074	G	759.3995	380.2034	742.3730	371.6901	6
4	440.3231	220.6652	423.2966	212.1519	468.3180	234.6627	451.2915	226.1494	L	631.3410	316.1741	614.3144	307.6608	5
5	539.3915	270.1994	522.3650	261.6861	567.3865	284.1969	550.3599	275.6836	V	518.2509	259.6321	501.2304	251.1188	4
6	668.4341	334.7207	651.4076	326.2074	696.4291	348.7182	679.4025	340.2049	E	419.1885	210.0979	402.1619	201.5846	3
7	783.4611	392.2342	766.4345	383.7209	811.4560	406.2316	794.4294	397.7184	D	290.1459	145.5766	273.1193	137.0633	2
8									R	175.1190	88.0631	158.0924	79.5498	1

#	a	a**	b	b**	Seq.	y	y**	y*	y***	#
1	74.0600	37.5337	102.0550	51.5311	T					11
2	211.1190	106.0631	239.1139	120.0606	H	1104.5354	552.7713	1087.5089	544.2581	10
3	298.1510	149.5791	326.1459	163.5766	S	*967.4785*	484.2418	950.4499	475.7286	9
4	429.1915	215.0994	457.1864	229.0968	M	*880.4464*	440.7259	863.4179	432.2126	8
5	542.2755	271.6414	570.2704	285.6389	I	*749.4040*	375.2056	732.3774	366.6923	7
6	657.3025	329.1549	685.2974	343.1523	D	*636.3199*	318.6636	619.2933	310.1503	6
7	744.3345	372.6709	772.3294	386.6683	S	*521.2930*	261.1501	504.2664	252.6368	5
8	831.3665	416.1869	859.3614	430.1844	S	*434.2605*	217.6341	417.2344	209.1208	4
9	944.4506	472.7289	972.4455	486.7264	L	*347.2285*	174.1181	330.2003	165.6043	3
10	1031.4826	516.2449	1059.4775	530.2424	S	*234.1445*	117.5761	217.1180	109.0628	2
11					K	*147.1128*	74.0600	130.0863	65.5469	1

Fig. S4. Mass spectrometric analysis for AREG binding protein. The MS data were obtained from three independent experiments. The results from 2DICAL analysis were shown in *A* and *C*. The MS peaks were developed in various combinations of axes; the *m/z* (*x* axis) and intensity axes (*y* axis) (*Upper Left*), the signal intensity (*Left*; *y* axis) and a box-and-whisker diagram (*Upper Right*), a grayscale intensity pattern of the RT (*Lower Left*; *x* axis), the *m/z* (*x* axis), and RT (*y* axis) (*Lower Right*). The results from Mascot search were shown in *B* and *D*. The results from *A* and *B* showed the MS peak of 493 *m/z* matched DDX5. The MS peak of 602 *m/z* matched AREG (*C* and *D*).

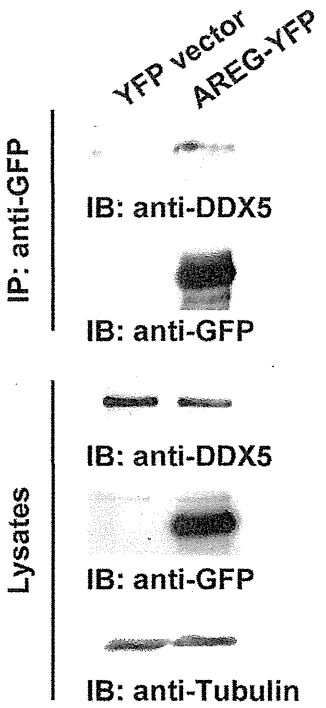

Fig. S5. DDX5 interacts with AREG. U2OS cells were transfected with YFP-vector or YFP-tagged AREG. Lysates were immunoprecipitated with anti-GFP. Immune complexes were subjected to immunoblot analysis with indicated antibodies.

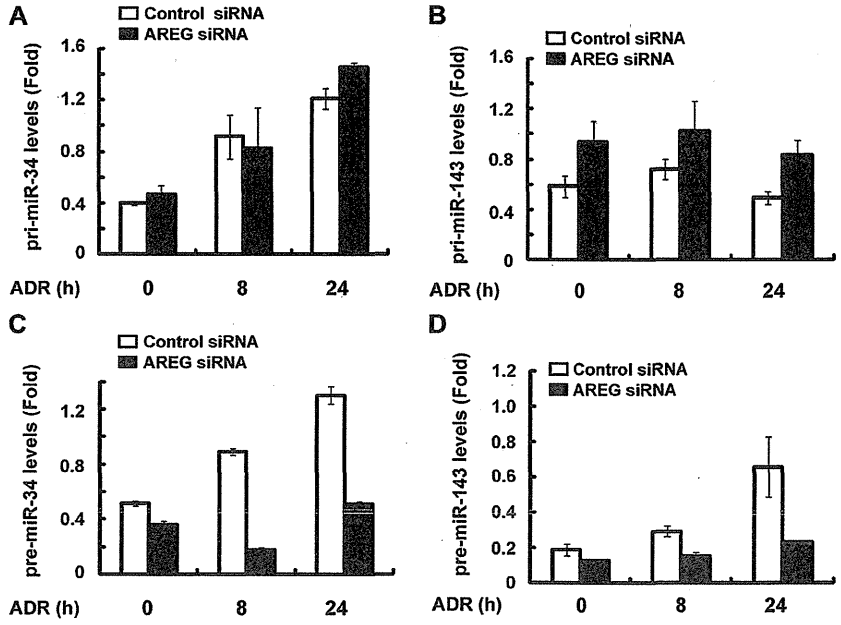

Fig. S6. AREG regulates biogenesis of microRNAs. U2OS cells were transfected with control siRNA or AREG siRNA and then treated with ADR for the indicated times. Total RNA was amplified with specific primers for pri-miR-34 (*A*), pri-miR-143 (*B*), pre-miR-34 (*C*), or pre-miR-143 (*D*). Data represent mean ± SD of relative induction.

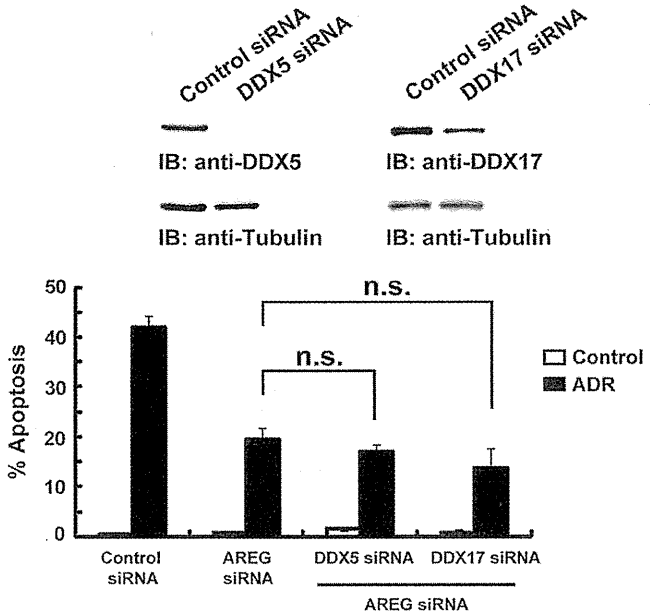

Fig. S7. AREG provokes apoptotic cell death via the microRNA processing. U2OS cells were cotransfected with AREG siRNA and DDX5 siRNA or DDX17 siRNA. Apoptosis induction was monitored by TUNEL assay. Knockdown efficiency of DDX5 or DDX17 was determined by immunoblot analysis. n.s., not significant.

Table S1. List of peptides from YFP-AREG immunocomplex

Protein ID	Relative ratio (compared with YFP-vector)	Sequence
AREG	5.57	THSMIDSSLSK
DDX5	1.47	APILIATDVASR
DDX5	1.48	LLQLVEDR
DDX5	1.32	QVSDLISVLR
DDX5	1.55	WNLDELPK

Cancer Medicine

Open Access

ORIGINAL RESEARCH

Galectin-7 as a potential predictive marker of chemo- and/or radio-therapy resistance in oral squamous cell carcinoma

Sho Matsukawa[1], Kei-ichi Morita[1,2], Ayako Negishi[1], Hiroyuki Harada[1], Yusuke Nakajima[1], Hiroaki Shimamoto[1], Hirofumi Tomioka[1], Kae Tanaka[1], Masaya Ono[3], Tesshi Yamada[3] & Ken Omura[1,2]

[1]Oral and Maxillofacial Surgery, Department of Oral Health Sciences, Graduate School of Medical and Dental Sciences, Tokyo Medical and Dental University, 1-5-45 Yushima, Bunkyo-ku, Tokyo 113-8510, Japan
[2]Department of Advanced Molecular Diagnosis and Maxillofacial Surgery, Hard Tissue Genome Research Center, Tokyo Medical and Dental University, 1-5-45 Yushima, Bunkyo-ku, Tokyo 113-8510, Japan
[3]Division of Chemotherapy and Clinical Research, National Cancer Center Research Institute, 5-1-1 Tsukiji, Chuo-ku, Tokyo 104-0045, Japan

Keywords
Formalin-fixed paraffin-embedded, galectin-7, liquid chromatography and mass spectrometry, oral squamous cell carcinoma

Correspondence
Kei-ichi Morita, Department of Advanced Molecular Diagnosis and Maxillofacial Surgery, Hard Tissue Genome Research Center, Tokyo Medical and Dental University, 1-5-45 Yushima, Bunkyo-ku, Tokyo 113-8510, Japan.
Tel: +81-3-5803-5510; Fax: +81-3-5803-0199;
E-mail: keiichi.m.osur@tmd.ac.jp

Funding Information
This study was supported by a Grant-in-Aid for Young Scientists (B-22791959) from the Japan Society for the Promotion of Science.

Received: 10 October 2013; Revised: 20 November 2013; Accepted: 26 December 2013

Abstract

Treatment of advanced oral squamous cell carcinoma (OSCC) requires the integration of multimodal approaches. The aim of this study was to identify predictors of tumor sensitivity to preoperative radiotherapy/chemotherapy for OSCC in order to allow oncologists to determine optimum therapeutic strategies without the associated adverse effects. Here, the protein expression profiles of formalin-fixed paraffin-embedded (FFPE) tissue samples from 18 OSCC patients, termed learning cases, who received preoperative chemotherapy and/or radiotherapy followed by surgery were analyzed by quantitative proteomics and validated by immunohistochemistry in 68 test cases as well as in the 18 learning cases. We identified galectin-7 as a potential predictive marker of chemotherapy and/or radiotherapy resistance, and the sensitivity and specificity of the galectin-7 prediction score (G7PS) in predicting this resistance was of 96.0% and 39.5%, respectively, in the 68 test cases. The cumulative 5-year disease-specific survival rate was 75.2% in patients with resistant prediction using G7PS and 100% in patients with sensitive prediction. In vitro overexpression of galectin-7 significantly decreased cell viability in OSCC cell line. Therefore, our findings suggest that galectin-7 is a potential predictive marker of chemotherapy and/or radiotherapy resistance in patients with OSCC.

doi: 10.1002/cam4.195

Introduction

Oral cancer is the sixth most common cancer worldwide, with an annual incidence of ~275,000 cases. However, unlike many other cancers, the incidence of oral cancer is increasing [1]. In Japan, the number of patients diagnosed with oral cancer was 2100 in 1975 and 6900 in 2005, and this number is estimated to increase to 7800 by 2015, when it will represent 1% of all cancer cases and approximately 40% of all head and neck cancer cases [2]. Histopathologically, squamous cell carcinoma (SCC) is the most common cancer of the oral cavity, accounting for >90% of all oral cancer cases. Despite recent improvements in multimodal therapies, the survival rate of these patients remains poor because of frequent locoregional and/or distant recurrences. These statistics highlight the urgent need for treatment alternatives [3].

Treatment of advanced head and neck SCC requires the integration of multimodal approaches. Interest in neoadjuvant chemotherapy has recently regenerated because of its survival benefits, particularly when a taxane–cisplatin–fluorouracil regimen is applied instead of the standard cisplatin–fluorouracil regimen [4–6]. Usually, tumor response to neoadjuvant chemotherapy predicts its response to radiotherapy. The prognostic indicators of favorable outcome would allow oncologists to make a more rational selection of therapeutic strategies without the unnecessary toxicities of neoadjuvant chemotherapy.

Over the past decade, gene expression in oral SCC (OSCC) has been studied extensively using microarray techniques. However, gene expression is not always correlated with the level of expression of the corresponding protein [7]. Furthermore, although the use of fresh material is required for most analytical approaches, human tissue samples are not always available in sufficient quantity. As an alternative, formalin-fixed paraffin-embedded (FFPE) tissue blocks can be routinely collected and stored as samples for research purposes after pathological diagnosis. A method of extracting proteins from FFPE tissues in the form of tryptic peptides was recently developed, and the methodology is compatible with a variety of mass spectrometry (MS)-based proteomics [8].

This study aimed to identify potential predictive markers of chemotherapy and/or radiotherapy resistance in patients with OSCC using quantitative proteomic analysis of FFPE biopsy tissues.

Patients and Methods

Patients

This retrospective study included 86 patients diagnosed with resectable OSCC and treated at the Tokyo Medical and Dental University Hospital Faculty of Dentistry (TMDU, Tokyo, Japan) between January 2001 and December 2011 (Table 1). The diagnosis was confirmed by histological examination of tissue biopsies surgically removed from the center of the cancerous tissue. The FFPE samples were fixed in formalin, embedded in paraffin, and stored at room temperature. Thereafter, all patients received preoperative chemotherapy and/or radiotherapy, followed by surgical primary tumor resection with or without neck dissection. After the chemotherapy and/or radiotherapy, treatment outcome was evaluated using the response evaluation criteria in the solid tumors (RECIST) guidelines. Cases of progressive disease (PD) or stable disease (SD) were assigned to the resistant group (Group R), whereas those who achieved a partial response (PR) or complete response (CR) were assigned to the sensitive group (Group S). This protocol was reviewed and approved by the Ethics Committee Board of the TMDU.

As learning cases, 18 biopsy samples were prepared (Table 1), including nine samples from Group R patients and nine samples from Group S patients. As test cases, 68 samples were prepared (Table 1), including 25 samples from Group R patients and 43 samples from Group S patients.

Preoperative chemotherapy and/or radiotherapy

Patients assigned to the S/R group received a daily fractional dose of radiotherapy (2 Gy; 5 days/week) for a total dose of 34–50 Gy using a 4MV LINAC (Varian, CA). Radiation was delivered to the primary tumor site and the cervical nodes for patients with nodal involvement. Concomitant chemotherapy with S-1 (Taiho Pharmaceutical Co., Tokyo, Japan) was orally administered twice a day after a meal for five consecutive days per week. The individual doses were calculated on the basis of body surface area (total 1000–3000 mg).

Patients assigned to the P/R group received a fractional daily dose of radiotherapy for a total dose of 50 Gy. Concomitant chemotherapy with carboplatin (CBDCA) or cisplatin (CDDP) was administered once a day using the selective intra-arterial infusion method via the superficial temporal artery [9]. The daily dose of CBDCA ranged from 10 to 30 mg, with a total dose of 495–725 mg. The daily dose of CDDP was 8 mg, with a total dose of 280 mg.

Patients in the pretreatment PF/R group received a daily fractional dose of radiotherapy for a total dose of 50 Gy. Concomitant chemotherapy with intravenous CDDP (80 mg/m^2), followed by 5-fluorouracil (5-Fu) (800 mg/m^2 per day) as a continuous 24-h infusion for five consecutive days, was administered.

Patients in the PF group received intravenous CDDP (60, 70, or 80 mg/m^2), followed by 5-Fu (600, 700, or 800 mg/m^2 per day) as a continuous 24-h infusion for five consecutive days. These patients received one or two cycles of treatment.

Patients in the pretreatment S group were administered oral S-1 twice a day after meals during the waiting period before surgery (total, 600–2100 mg).

Finally, patients in the pretreatment R group only received a daily fractional dose of radiotherapy (2.5 Gy for 4 days/week), with a total dose of 40 Gy.

Peptide extraction

The proteins were extracted from the FFPE samples in the form of tryptic peptides using the Liquid Tissue MS Protein Partitioning Kit (Expression Pathology, Rockville, MD) according to the manufacturer's protocol. The

Table 1. Clinical characteristics and expression profile of galectin-7.

Patient no.	Case	Group	Gender	Age	Primary site	Differentiation	TN	Stage	G7S	G7NL	Prediction score	Pre C/R	Response to therapy
1	Learning	Group R	F	61	Mandibula	Grade 2	T4N1	4A	29	2	−2.78	PF + S/R	NC
2	Learning	Group R	M	60	Maxillary sinus	Grade 3	T3N2c	4C	0	0	−1.97	P/R	NC
3	Learning	Group R	M	50	Floor of mouth	Grade 2	T3N2b	4A	45.5	2	−1.82	S/R	NC
4	Learning	Group R	M	57	Tongue	Grade 1	T2N1	3	48.4	2	−1.65	S/R	NC
5	Learning	Group R	M	79	Tongue	Grade 2	T3N1	3	48.4	2	−1.65	S/R	NC
6	Learning	Group R	M	32	Tongue	Grade 1	T2N2b	4A	31.5	1	−1.38	S/R	NC
7	Learning	Group R	M	57	Tongue	Grade 1	T3N2b	4A	57.7	2	−1.10	PF + S/R	PD
8	Learning	Group R	M	68	Mandibula	Grade 2	T4N2b	4A	44.9	1	−0.61	PF	NC
9	Learning	Group R	M	47	Tongue	Grade 2	T2N0	2	46.6	1	−0.51	PF	NC
10	Learning	Group S	M	72	Floor of mouth	Grade 2	T3N2c	4A	72.5	2	−0.25	S/R	PR
11	Learning	Group S	M	50	Tongue	Grade 1	T2N0	2	34.6	0	0.04	S	PR
12	Learning	Group S	M	82	Tongue	Grade 1	T2N0	2	56.8	1	0.09	S	PR
13	Learning	Group S	M	59	Tongue	Grade 2	T3N0	3	61.6	0	1.61	S/R	PR
14	Learning	Group S	M	61	Tongue	Grade 1	T2N0	2	66.5	0	1.90	S	PR
15	Learning	Group S	M	68	Lower gingiva	Grade 1	T2N0	2	66.6	0	1.90	S/R	PR
16	Learning	Group S	M	76	Lower gingiva	Grade 1	T2N2b	4A	78.7	0	2.60	S	PR
17	Learning	Group S	M	29	Tongue	Grade 2	T2N0	2	80.4	0	2.70	S/R	PR
18	Learning	Group S	M	53	Lower gingiva	Grade 1	T2N1	3	83.3	0	2.87	S	PR
19	Test	Group R	M	58	Mandibula	Grade 2	T4N2b	4A	24.1	2	−3.06	S	NC
20	Test	Group R	M	70	Floor of mouth	Grade 2	T2N2c	4A	4.53	1	−2.95	R	NC
21	Test	Group R	M	57	Maxillary sinus	Grade 2	T4N1	4B	11.4	1	−2.55	P/R	NC
22	Test	Group R	F	66	Maxillary sinus	Grade 2	T3N2b	4A	12.7	1	−2.47	S/R	NC
23	Test	Group R	M	45	Tongue	Grade 3	T3N2b	4A	34.4	2	−2.46	PF	NC
24	Test	Group R	M	60	Tongue	Grade 2	T4N2c	4A	35.3	2	−2.41	S	NC
25	Test	Group R	F	81	Lower gingiva	Grade 3	T4N0	4A	16.6	1	−2.25	R	NC
26	Test	Group R	F	72	Buccal mucosa	Grade 1	T4N2b	4A	0	0	−1.97	R	NC
27	Test	Group R	M	67	Upper gingiva	Grade 3	T2N1	3	0.6	0	−1.93	S	NC
28	Test	Group R	M	53	Soft palate	Grade 3	T4N1	4A	8.14	0	−1.50	R	NC
29	Test	Group R	M	59	Buccal mucosa	Grade 2	T4N2b	4A	31.6	1	−1.38	R	NC
30	Test	Group R	M	53	Mandibula	Grade 1	T4N2b	4A	33.4	1	−1.27	R	NC
31	Test	Group R	M	68	Mandibula	Grade 2	T4N2b	4A	56.1	2	−1.20	S	NC
32	Test	Group R	F	54	Tongue	Grade 2	T2N2b	4A	37	1	−1.06	S	NC
33	Test	Group R	F	52	Lower gingiva	Grade 2	T4N2c	4A	60.8	2	−0.93	S	NC
34	Test	Group R	M	61	Retromolar trigone	Grade 1	T4N1	4A	40.7	1	−0.85	S	NC
35	Test	Group R	M	41	Tongue	Grade 3	T2N2c	4A	20.2	0	−0.79	R	NC
36	Test	Group R	M	66	Mandibula	Grade 1	T4N2b	4A	43	1	−0.72	S	NC
37	Test	Group R	M	74	Lower gingiva	Grade 2	T4N2b	4A	68	2	−0.51	S	NC
38	Test	Group R	M	69	Tongue	Grade 2	T3N2b	4A	25.8	0	−0.47	PF	NC
39	Test	Group R	M	57	Mandibula	Grade 1	T4N0	4A	31.8	0	−0.12	R	NC
40	Test	Group R	M	64	Tongue	Grade 2	T3N2c	4A	75	2	−0.10	PF	NC
41	Test	Group R	M	62	Maxila	Grade 2	T4N1	4A	33	0	−0.05	S/R	NC
42	Test	Group R	M	57	Tongue	Grade 2	T2N0	2	33.1	0	−0.04	S/R	NC
43	Test	Group R	M	64	Tongue	Grade 2	T3N2b	4A	72.4	1	0.99	S	NC
44	Test	Group S	M	57	Maxillary sinus	Grade 2	T3N0	3	0.7	2	−4.42	P/R	PR
45	Test	Group S	M	52	Lower gingiva	Grade 2	T2N2b	4A	1.35	2	−4.38	S/R	PR
46	Test	Group S	M	55	Tongue	Grade 3	T3N2b	4A	6.63	1	−2.83	PF	PR
47	Test	Group S	M	74	Upper gingiva	Grade 3	T4N2b	4A	9.94	1	−2.64	S/R	PR
48	Test	Group S	M	62	Tongue	Grade 3	T3N0	3	10.9	1	−2.58	S/R	PR
49	Test	Group S	M	71	Buccal mucosa	Grade 3	T3N2b	4B	39.9	2	−2.14	PF	PR
50	Test	Group S	F	76	Upper gingiva	Grade 2	T4N0	4A	0	0	−1.97	S/R	PR
51	Test	Group S	F	52	Tongue	Grade 3	T3N0	3	2.1	0	−1.85	S/R	PR
52	Test	Group S	M	50	Tongue	Grade 1	T2N0	2	6.2	0	−1.61	S/R	PR

Table 1. Continued.

Patient no.	Case	Group	Gender	Age	Primary site	Differentiation	TN	Stage	G7S	G7NL	Prediction score	Pre C/R	Response to therapy
53	Test	Group S	M	49	Tongue	Grade 2	T3N1	3	27.9	1	−1.60	PF	PR
54	Test	Group S	M	48	Lower gingiva	Grade 1	T4N0	4A	31.1	1	−1.41	S/R	PR
55	Test	Group S	M	62	Lower gingiva	Grade 2	T3N2b	4A	33.1	1	−1.29	S/R	PR
56	Test	Group S	M	58	Floor of mouth	Grade 2	T2N2c	4A	11.9	0	−1.28	R	PR
57	Test	Group S	M	61	Upper gingiva	Grade 3	T4N0	4A	12.2	0	−1.26	P/R	PR
58	Test	Group S	M	59	Floor of mouth	Grade 2	T4N2c	4A	33.7	1	−1.26	PF	PR
59	Test	Group S	F	67	Tongue	Grade 2	T2N2c	4A	34.8	1	−1.19	PF	PR
60	Test	Group S	F	64	Upper gingiva	Grade 2	T3N0	3	37.1	1	−1.06	S/R	PR
61	Test	Group S	M	58	Lower gingiva	Grade 2	T3N1	3	59	2	−1.03	S/R	PR
62	Test	Group S	M	54	Lower gingiva	Grade 2	T2N2b	4A	16.7	0	−1.00	S/R	PR
63	Test	Group S	M	69	Tongue	Grade 2	T3N0	3	20.8	0	−0.76	S/R	PR
64	Test	Group S	M	65	Tongue	Grade 1	T3N0	3	26.5	0	−0.43	PF	PR
65	Test	Group S	F	40	Tongue	Grade 2	T2N2b	4A	27.9	0	−0.35	S/R	PR
66	Test	Group S	M	54	Lower gingiva	Grade 2	T4N0	4A	28.3	0	−0.32	R	PR
67	Test	Group S	M	55	Tongue	Grade 1	T3N1	3	30.9	0	−0.18	S/R	PR
68	Test	Group S	M	59	Floor of mouth	Grade 2	T2N0	2	52.3	1	−0.17	S/R	PR
69	Test	Group S	M	67	Floor of mouth	Grade 2	T4N1	4A	31.1	0	−0.16	S/R	PR
70	Test	Group S	F	64	Lower gingiva	Grade 1	T4N1	4A	35.6	0	0.10	S/R	PR
71	Test	Group S	M	65	Tongue	Grade 1	T3N1	3	80	2	0.19	PF	PR
72	Test	Group S	M	66	Floor of mouth	Grade 2	T3N0	3	60.7	1	0.31	PF	PR
73	Test	Group S	M	65	Retromolar trigone	Grade 2	T2N0	2	41.4	0	0.44	R	PR
74	Test	Group S	M	75	Upper gingiva	Grade 3	T4N2c	4A	41.4	0	0.44	S/R	PR
75	Test	Group S	F	62	Maxila	Grade 1	T4N0	4A	42.6	0	0.51	PF/R	PR
76	Test	Group S	F	52	Tongue	Grade 2	T2N0	2	43.1	0	0.53	S/R	PR
77	Test	Group S	M	59	Tongue	Grade 1	T3N2c	4A	47	0	0.76	R	PR
78	Test	Group S	M	48	Tongue	Grade 2	T3N2b	4A	51.5	0	1.03	PF	PR
79	Test	Group S	M	62	Buccal mucosa	Grade 2	T2N0	2	52.8	0	1.10	S/R	PR
80	Test	Group S	F	46	Tongue	Grade 2	T3N0	3	54.3	0	1.18	S/R	PR
81	Test	Group S	M	45	Lower gingiva	Grade 1	T4N1	4A	54.4	0	1.19	S/R	PR
82	Test	Group S	M	45	Floor of mouth	Grade 1	T2N0	2	55.2	0	1.24	S/R	CR
83	Test	Group S	M	56	Tongue	Grade 3	T3N0	3	55.9	0	1.28	S/R	PR
84	Test	Group S	F	62	Lower Gingiva	Grade 2	T3N0	3	60.2	0	1.53	R	PR
85	Test	Group S	M	58	Soft palate	Grade 2	T3N0	3	69.9	0	2.09	S/R	PR
86	Test	Group S	M	68	Lower gingiva	Grade 1	T4N0	4A	71.6	0	2.19	S/R	PR

Group R, resistant group; Group S, sensitive group; M, male; F, female; Pre C/R, preoperative chemotherapy and/or radiotherapy; S/R, S-1 + radiation; P/R, carboplatin or cisplatin + radiation; PF/R, cisplatin and 5-fluorouracil + radiation; PF, cisplatin and 5-fluorouracil; S, S-1; R, radiation; CR, complete remission; PR, partial response; SD, stable disease; PD, progressive disease.

extracted peptides were desalted through a C18 ZipTip (Millipore, Billerica, MA).

Liquid chromatography–mass spectrometry

Eighteen samples (nine from Group R and nine from Group S) were blinded, randomized, and measured in duplicate with a linear gradient of 0–80% acetonitrile in 0.1% formic acid at a speed of 200 nL/min for 60 min using a nano-flow high-performance liquid chromatography (HPLC; NanoFrontier nLC; Hitachi High-technologies, Tokyo, Japan) that was connected to a triple time-of-flight mass spectrometer (5600 Triple TOF; AB Sciex, Framingham, MA). The system detected peptide peaks every 1 sec, with a mass-to-charge ratio (m/z) ranging from 400 to 1600. The MS peaks were detected, normalized, and quantified using in-house 2DICAL (two-dimensional image-converted analysis of liquid chromatography and mass spectrometry) software as described previously [10]. A serial identification (ID) number was assigned to each MS peak from ID1 to ID70510.

Protein identification by MS/MS

The MS/MS spectra were aligned with a tolerance of ±0.5 m/z and a retention time (RT) of ±0.4 min. Then,